Expert-based prior uncertainty analysis of gridded water balance components
Application to the irrigated Hindon River Basin, India

Mourad, Roya; Schoups, Gerrit; Bastiaanssen, Wim; Kumar, D. Nagesh

DOI
10.1016/j.ejrh.2024.101935

Publication date
2024

Document Version
Final published version

Published in
Journal of Hydrology: Regional Studies

Citation (APA)
Mourad, R., Schoups, G., Bastiaanssen, W., & Kumar, D. N. (2024). Expert-based prior uncertainty analysis of gridded water balance components: Application to the irrigated Hindon River Basin, India. *Journal of Hydrology: Regional Studies*, *55*, Article 101935. https://doi.org/10.1016/j.ejrh.2024.101935

Journal of Hydrology: Regional Studies 55 (2024) 101935

Contents lists available at ScienceDirect

Journal of Hydrology: Regional Studies

journal homepage: www.elsevier.com/locate/ejrh

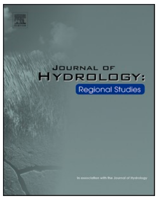

Expert-based prior uncertainty analysis of gridded water balance components: Application to the irrigated Hindon River Basin, India

Roya Mourad [a,*], Gerrit Schoups [a], Wim Bastiaanssen [a,b], D. Nagesh Kumar [c,d]

[a] *Department of Water Management, Faculty of Civil Engineering and Geosciences, Delft University of Technology, Stevinweg 1, 2628 CN Delft, the Netherlands*
[b] *Hydrosat, Wageningen 6708 PW, the Netherlands*
[c] *Department of Civil Engineering, Indian Institute of Science, Bengaluru, Karnataka 560012, India*
[d] *Lyles School of Civil Engineering , Purdue University, West Lafayette, IN 47907, USA*

ARTICLE INFO

Keywords:
Precipitation
Evaporation
Water storage
Inter-product differences
Grid-scale uncertainty
Spatio-temporal variations
Seasonal water balance

ABSTRACT

Study region: Hindon River Basin, North India.
Study focus: Accurate estimation of water balance components is crucial for water management applications yet challenging due to errors in monthly gridded water balance data products. Error and uncertainty quantification is especially important in the absence of extensive in-situ data. This paper presents a prior uncertainty analysis for such situations consisting of two components: (i) quantification of prior uncertainties using metrics that quantify errors in individual products and variability and consistency between products, and (ii) reduction of prior uncertainties by eliminating unrealistic water balance estimates.
New hydrological insights for the region: Grid-scale inter-product uncertainty or variability, computed as the coefficient of variation (CV, %) at various temporal scales, reveals discrepancies between water balance products due to a combination of factors, including methodological differences, inherent spatial variability, data sources, and resolution disparities. At the mean annual scale, P fluxes display a lower grid-scale inter-product uncertainty (5–9 %) than ET (20–55 %), while the ΔTWS from GRACE solutions show a moderate mean annual grid-scale inter-product uncertainty (15–19 %). Grid-scale inter-product uncertainties of ΔSMS for July – representing the onset of the monsoon season – are high (CV = 54–122 %), indicating that the uncertainty in estimates of this component may have a large impact on water balance analyses. P fluxes exhibited fewer spatio-temporal uncertainties (R^2 above 0.8) than ET fluxes (R^2 less than 0.75). The exclusion of the unreliable data sets resulted in (a) reducing uncertainties in input water balance components with triple collocation range shifting from 15–38 to 17–23 mm/month for ET and from 16–52 to 11–23 mm/month for P, (b) obtaining updated prior estimates of seasonal water balance. The updated priors of water balance variables per season suggest a net basin outflow (from −318 to −57 mm/season) during the monsoon (rainy) season and net basin inflow (from −38 to 330 mm/season) during the non-monsoon (dry) season, the latter related to surface-water imports from outside the basin. All GRACE data sets exhibit a regional long-term decreasing trend in total water storage (ranging from −31 to −61 mm/year), qualitatively confirming previously documented unsustainable groundwater depletion in the basin. Prior ranges and

---

[*] Corresponding author.
E-mail address: R.Mourad@tudelft.nl (R. Mourad).

https://doi.org/10.1016/j.ejrh.2024.101935
Received 23 December 2023; Received in revised form 8 August 2024; Accepted 10 August 2024

uncertainties for all water balance variables reported here can be used as input into a posterior analysis that uses in-situ data for locally calibrating (bias-correcting, noise-filtering) and further updating the prior estimates.

1. Introduction

The maturity of remote sensing science and algorithm developments for estimating the water balance components has given rise to multiple open-access remote sensing and reanalysis data sets with a wide range of spatio-temporal resolutions. These data sets have been widely used in several applications ranging from irrigation management (Melton et al., 2012), water accounting (Hessels et al., 2022; Karimi et al., 2013), and drought monitoring (Otkin et al., 2014; Sheffield and Wood, 2007), to reporting sustainable development (SDGs) (Vanham et al., 2018) and water footprint indicators (Mekonnen and Hoekstra, 2011), thus providing valuable insights into hydrological processes (Lakshmi, 2016). Despite these data sets' widespread and extensive potential, all have various levels of systematic (bias) and random (noise) errors. Accordingly, there is a need to quantify and investigate the uncertainties in these data sets before their use in hydrological applications.

Uncertainties in water balance data sets have been investigated in a multitude of scientific studies, either focusing on multiple water balance components simultaneously (Gao et al., 2010; Sheffield et al., 2009) or on specific water balance fluxes such as Precipitation (P) (Gehne et al., 2016; Herold et al., 2017; Sun et al., 2018)), Evapotranspiration (ET) (Jaafar et al., 2022; Pan et al., 2020; Sriwongsitanon et al., 2020; Weerasinghe et al., 2020), soil moisture storages (SMS) (Albergel et al., 2012; Colliander et al., 2017; Ma et al., 2019) and total water storage (TWS) (Biancamaria et al., 2019; Scanlon et al., 2016)). P is the most explored component among the water balance data sets due to its importance in weather, climate, and hydrological forecasting (Sarojini et al., 2016). SMS and TWS are the next most studied due to their importance in climate models (Koster and Suarez, 2001; Walker and Houser, 2001) and global change modeling (Henderson-Sellers, 1996; Taylor et al., 2013). ET was the least investigated component until recently, when an emerging focus on water management has given rise to a plethora of research and RS-ET product development (Anderson et al., 2015; Bastiaanssen et al., 1998, 1993; FAO, 2020; Feddes et al., 1993; Guerschman et al., 2009; Mu et al., 2011; Senay et al., 2013). Some studies show that among the water balance components, ET has the largest error, resulting in the deviation from water balance closure (Abera et al., 2017; Soltani et al., 2020), while other studies concluded that the largest errors are either caused by P (Sheffield et al., 2009; Wong et al., 2021) or TWS from GRACE (Aires, 2014; Long et al., 2014). These contrasting conclusions necessitate the assessment of the water balance component data sets prior to their incorporation in water balance analyses.

While the hydrological community recognizes the significance of quantifying uncertainties in water balance data sets, there is currently no standardized method for error estimation. Bias and random errors in modeled water balance components are commonly quantified through direct validation against in-situ measurement reference data. Ground-based observations exhibit the greatest reliability, but even the most frequently and conceivably best-measured components – P from rain gauges, ET from Eddy Covariance (EC), lysimeters, or scintillometers, river discharge from stream gauges, TWS from well observations (in regions with extensive observations and where groundwater storage dominates the TWS signal) – still carry significant uncertainty due to unpredictable random errors (Kumar et al., 2017), and data errors (Massman and Lee, 2002). Other approaches quantify the relative uncertainties in water balance components by comparing them to a reference data set (Gao et al., 2010; Sheffield et al., 2009), other models (Koppa and Gebremichael, 2017; Scanlon et al., 2019), or by using inter-product comparisons (Parinussa et al., 2014; Weerasinghe et al., 2020), based on a triple collocation or three-cornered hat method (Alemohammad et al., 2015; Khan et al., 2018; Yang et al., 2022). In addition, methods such as sensitivity analysis (Seo et al., 2010), uncertainty propagation (Cawse-Nicholson et al., 2020; Hong et al., 2006), and calculation of the coefficient of variation across multi-data sources of the same variable (Zhang et al., 2018) are also utilized. Another category of studies encompasses water balance closure methods developed to produce reliable and corrected water balance estimates, including approaches such as Proportional Redistribution (PR) (Abolafia-Rosenzweig et al., 2021), Constrained Kalman Filter (CKF) (Pan and Wood, 2006; Zhang et al., 2018), Multiple Collocation (MCL) (Abhishek et al., 2021), and probabilistic data fusion methods (Schoups and Nasseri, 2021). Some of the mentioned water balance closure methods have reduced uncertainties in input water balance data sets through bias correction before enforcing the water balance (Pan and Wood, 2006). Accounting for uncertainties in input data sets improves the accuracy of the corrected water balance estimates in water balance closure methods. Luo et al. (2023), for instance, have considered using high-precision water balance components before enforcing the water balance closure, underscoring the importance of considering the uncertainties of input data sets for obtaining more reliable and accurate water balance closure results.

This study expands on previous attempts to quantify and reduce uncertainties in the water balance components. The focus of this analysis is twofold. First, we develop and apply an expert-based prior uncertainty analysis framework for water balance variables. The term "prior" refers to the fact that our methodology does not rely on in-situ data, specifically river discharge data, which is often unavailable or inaccessible in many basins worldwide. Instead, we employ a combination of physical reasoning and uncertainty metrics to quantify and partially reduce prior uncertainties. This is achieved by evaluating (i) the prior plausibility of individual water balance variables using limited in-situ data, physical reasoning, and inter-product comparisons, and (ii) the prior plausibility of multi-variable combinations by assessing their representation of the long-term physically constrained seasonal water balance. Second, we apply the proposed approach to a monsoon-influenced and irrigated basin, the Hindon River basin of northern India – a tributary of the Yamuna River – that suffers from groundwater overexploitation and depends on external surface water imports. We present the first study on the Hindon basin, providing insights into the basin's major hydrological processes and their associated uncertainties.

To achieve the above goals, we structure the paper in the following manner: In Section 2, we outline our methodology for quantifying and reducing prior uncertainties; in Sections 3 and 4, we summarize the data sets used to apply the proposed framework to a case study of the Hindon Basin in Northern India, and in Section 5 we present and discuss the main findings. We conclude the paper with Section 6 by providing perspectives for future water balance analyses.

The reader should note that as part of this multi-temporal analysis, all water balance variables, including the rate of changes in total water storage (TWS) and soil moisture storage (SMS), are expressed per unit of time at monthly, yearly, seasonal, and/or long-term scales. Throughout the paper, for ΔSMS/Δtime and ΔTWS/Δtime, we employ the abbreviated notations ΔSMS and ΔTWS to maintain conciseness, while the exact time period is indicated by the context in which they are used.

2. Prior uncertainty analysis

In the following subsections, we outline the proposed framework for quantifying and partially reducing prior uncertainties associated with water balance component data sets in the absence of in-situ data (i.e., river discharge and external surface water imports).

2.1. Quantifying prior uncertainties

The agreement between the various water balance components data sources is thoroughly evaluated through a combination of diagnostic plots to assess the temporal and magnitude consistency among the data sources for each variable (P, ET, ΔSMS, ΔTWS) at monthly and annual time steps. We use statistical metrics to quantify the uncertainty of these data sets along three dimensions (Table 1): spatio-temporal consistency between product pairs, grid-scale inter-product uncertainty, and random errors in individual data products.

We assess the spatio-temporal consistency between pairs of data products by the coefficient of determination (R^2) of the linear regression between paired-pixel values for the long-term mean annual and monthly estimates of P and ET. Across all products, we quantify the grid-scale inter-product uncertainty for long-term mean annual estimates describing each water balance variable (P, ET, and ΔTWS) by calculating the coefficient of variation (CV, %) at each grid cell across the data sets. Given the dynamic nature of the ΔSMS component and its potential impact on the water balance at shorter timescales, we assess the inter-product uncertainty by computing the CV (%) at a grid-level for July, representing the onset of the monsoon season in the Hindon River Basin (Section 4).

We further employ the triple collocation method (TC) (Stoffelen, 1998) to evaluate uncertainties in individual products. TC is interchangeably used with the intercomparison approach in the sense that both assess the data sets' relative uncertainties without presuming the superiority of one over the other. TC is a common error estimation technique that provides estimates of the random error variances (σ^2) associated with each data set in question, useful when the true value of the variable is unknown but multiple estimates are available. The TC error model assumes that each data set (e.g., A, B, C) can be represented as a linear function of the true value (Θ) with additive (α) and multiplicative (β) biases, along with zero-mean random noise. Estimating the basic (classical) TC error is commonly done either through rescaling the data sets to a reference data set (removing α and β) or based on the covariances between the data sets, with the former used in this analysis. The error variance for all possible triplet combinations of four P, six ET, five SMS, and four TWS products is calculated, and we report the final TC error (in mm/month) as the mean standard deviation (σ) for all possible triplets where a data set appears. A low (σ) for a specific data set denotes a small random error. In this analysis, achieving true independency in the water balance data sets was challenging due to data availability constraints. Some of the data sets may violate TC's major assumptions of data sets' independence due to shared input data, modeling approaches, and parameterization, which can lower the TC error estimates (Yilmaz and Crow, 2013). Additionally, increasing the number of data sets typically increases the inter-model variability. However, using an ensemble of data sets for each water balance component (>3 data sets) helps overcome the potential impact of extreme individual triplets on the error estimation. In this context, we employ the basic TC to assess the relative uncertainties between the data sets, regardless of the magnitude of their random errors. A higher range of errors, even with potential bias due to violations of the TC's major assumption, can still serve as an approximate measure and help reveal inconsistent data sets. TC is used here to complement/support conclusions drawn from the other statistical metrics (R^2 and CV (%)).

In R^2 formula, A_i represents values in data set A, B_i represents values in data set B, $\underline{A_i}$ is the mean of values in data set A, and n is the number of data points in the paired data set A and B. In the CV formula, s_i and $\overline{x_i}$ represent the standard deviation and mean of all evaluated water balance estimates for each variable (P, ET, ΔSMS, ΔTWS) at the ith grid cell. In the triple collocation error equations, the brackets represent the temporal mean, A, B, and C are the three data sets, A_s, B_s, C_s are the three data sets scaled to the mean and

Table 1
Statistical metrics used for uncertainty assessment.

Uncertainty aspect	Metric	Formula
Spatio-temporal consistency between product pairs	Coefficient of determination (R^2)	$R^2(A,B) = 1 - \frac{\sum_{i=1}^{n}(A_i - B_i)^2}{\sum_{i=1}^{n}\left(A_i - \underline{A_i}\right)^2}$
Grid-scale variability across all products	Coefficient of variation (CV, %)	$CV_i = \frac{s_i}{\overline{x}_i}100$
Random errors in individual data products	Triple collocation error (TC) (mm/month)	$\sigma_A = \sqrt{<(A - B_s)(A - C_s)>}$ $\sigma_B = \sqrt{<(B - A_s)(B - C_s)>}$ $\sigma_C = \sqrt{<(C - A_s)(C - B_s)>}$

standard deviation of the reference data set (Scipal et al., 2008). The rescaling procedure is applied to ensure the error orthogonality assumption of TC is preserved, and the system is solvable.

2.2. Reducing prior uncertainties

We follow a proactive approach based on multiple lines of evidence to a priori exclude data sets with significant bias. The approach is applied to P and ET products to exclude the data set(s) that yield unrealistic individual water balance estimates and to combinations of all products (P, ET, ΔTWS) that yield unrealistic estimates of the seasonal water balance.

The P products are evaluated against rain gauges using the point-to-pixel approach at a monthly temporal scale for the periods where the observed data are available. This approach assumes that the rain gauge observations are representative values over a corresponding grid cell (Baez-Villanueva et al., 2018; Zambrano-Bigiarini et al., 2017). The ability of the satellite-based P to capture the observed P at each weather station is assessed using three statistical indices: Pearson's linear correlation (r), Root Mean Square Error (RMSE), and percentage bias (pBIAS). These indices are commonly used for rainfall evaluation (Ebert et al., 2007; Xu et al., 2017; Zhang et al., 2019). In addition to their relative performance against limited in-situ data, unreliable P products are excluded based on a comprehensive prior uncertainty analysis (Section 2.1).

The ET products are evaluated by comparing them to a physically-based benchmark, which builds upon the expectation that

Table 2
Overview of water balance data sets used in this study. The data type column distinguishes between Remote Sensing (RS), Ground-Based Measurements (GBM), Water Balance (WB), and Land Surface Models (LSM). Data sources marked with an asterisk (*) were processed as part of this study (processing details can be found in the Supplementary Material), and unmarked data sources were collected from either Google Earth Engine or other platforms.

Precipitation (P)			
Data Type	Data Source	Original (Resampled) Spatial resolution	Study period
RS and GBM	TRMM TMBA (TRMM3B43 v7)	0.25° (0.05°)	2003–2019
RS and GBM	CHIRPS v2.0	0.05° (0.05°)	2003–2019
RS and GBM	GPM (IMERG) 3IMERGDF (v06)	0.1° (0.05°)	2003–2019
Merged	MSWEP v2.8	0.1° (0.05°)	2003–2019
Evapotranspiration (ET)			
Data Type	Data Source	Original (Resampled) Spatial resolution	Study period
RS	pyWaPOR v2.6 * (2-layer PM, ETLook) (https://www.fao.org/aquastat/py-wapor/index.html)	250 m (1Km)	2003–2021
RS	SSEBop v4 (1-layer PM, SEB) (MODIS-based version, SSEBop (a))	1Km(1Km)	2003–2021
RS	Landsat Collection 2 Level−3 Provisional Actual Evapotranspiration (SSEBop) (Landsat-based version, SSEBop (b))	30 m (1Km)	2003–2021
RS	eeSEBAL* (SEB, Single-source residual)	30 m (1Km)	2003–2021
RS	MOD16 A2 (v006) (3-layer PM) (GEE image collection: MODIS/006/MOD16A2)	500 m (1Km)	2003–2021
RS	CMRSET	5Km (1Km)	2003–2012
RS	ALEXI (SEB, Two-source residual)	5Km (1Km)	2003–2015
Soil Moisture Storage (SMS)			
Data Type	Data Source	Original (Resampled) Spatial resolution	Study period
LSM	GLDASv2.2 (GEE image collection: NASA/GLDAS/V022/CLSM/G025/DA1D)	∼27Km(4Km)	2003–2021
LSM	ERA5 (GEE image collection: ECMWF/ERA5_LAND/MONTHLY)	∼11Km(4Km)	2003–2021
RS and WB	SMAP (GEE image collection: NASA_USDA/HSL/SMAP_soil_moisture)	∼25Km(4Km)	2015–2020
RS and WB	SMOS (GEE image collection: NASA_USDA/HSL/soil_moisture)	∼25Km(4Km)	2010–2020
RS	pyWaPOR*	250 m(4Km)	2003–2021
WB	Terra Climate (GEE image collection: IDAHO_EPSCOR/TERRACLIMATE)	4Km(4Km)	2003–2021
Total Water Storage (TWS)			
Data Type	Data Source	Spatial resolution	Study period
Mascon (MAS)(GRACE-JPL)	GRACE Monthly Mass Grids – Global Mascon (CRI Filtered) (GEE image collection: NASA/GRACE/MASS_GRIDS/MASCON_CRI)	3°	2002–2016
Spherical harmonic (GRACE-CSR, GRACE-JPL, and GRACE GFZ)	GRACE Monthly Mass Grids – Land (GEE image collection: NASA/GRACE/MASS_GRIDS/LAND)	1°	2002–2016

realistic ET estimates should follow the temporal dynamics of irrigation water applications (i.e., high ET estimates when irrigation is conducted) and be higher for irrigated crops than other land use elements such as non-vegetated urban areas and rainfed crops. In support of this benchmark, exclusions of unreliable ET products are based on the consistency analysis (Section 2.1) and supporting literature.

Additionally, we quantitatively assess the impact of excluding P and ET on the triple collocation error.

Finally, the plausibility of product combinations is assessed by disaggregating and applying the water balance by season (dry vs. rainy) for a long-term period using unique combinations of P, ET, and ΔTWS. The combinations that don't provide realistic estimates of the seasonal water balance are excluded from the analysis. At the basin level, the water balance can be expressed as:

$$0 \approx P - ET - Q_{out} + Q_{in} - \Delta TWS \tag{1}$$

where Q_{out} represents total outflow across the basin boundaries, including river discharge at the basin's outlet and any groundwater outflow and Q_{in} is total inflow across the basin boundaries, including groundwater inflows, as well as external irrigation water imports from outside the basin. The term ΔTWS is the change in total water storage (surface and subsurface).

The seasonal disaggregation of the water balance is based on precipitation patterns. For example, for the case study (Section 4), we define a monsoon or wet season from June to September, and a non-monsoon or dry season from October to May. Based on this, Eq. 1 can then be rearranged as:

$$Q_{in} - Q_{out} \approx \Delta TWS - P + ET = \varepsilon = Q_{net} \tag{2}$$

Often, measurements of Q_{in} and Q_{out} are unavailable in data-scarce regions. Nevertheless, in conjunctively irrigated basins with strong seasonality (e.g., monsoon climate), it may be possible to put reasonable constraints on the seasonal value of the net flows ($\varepsilon = Q_{net} = Q_{in} - Q_{out}$) (e.g., positive or negative), which in turn provides constraints on valid combinations of seasonal values for P, ET, and ΔTWS. In the non-monsoon season, we reasonably expect to have positive net inflows (i.e., Q_{in} to exceed Q_{out}), suggesting that valid combinations of P, ET, ΔTWS products should satisfy the constraint that $Q_{in} > Q_{out}$ or $\varepsilon > 0$. Conversely, in the monsoon season we expect valid combinations of P, ET, and ΔTWS products to satisfy the constraint of $Q_{in} < Q_{out}$ or $\varepsilon < 0$. In reality, ε combines uncertainties from P, ET, and ΔTWS. As such, we quantitatively study how the uncertainties of different combinations of P, ET, and ΔTWS control the value of ε by analyzing the impact of excluding unreliable individual water balance components (P and ET) data sets on ε per season. This is achieved through the computation of the ensemble of long-term average ε disaggregated by season for the three scenarios, using (i) inputs of all water balance components data sets, before any exclusion, including 4 P, 7 ET, and 4 ΔTWS, resulting in 112 combinations, (ii) after excluding all combinations containing the identified unreliable P and ET data sets based on multiple criteria described above, (iii) after exclusion of combinations showing unrealistic ε. Scenarios (i) and (ii) essentially serve as an alternative to a formal sensitivity analysis of excluding the individual P and ET data set(s). For the third scenario, we use seasonal constraints of $\varepsilon > -50$ mm /non-monsoon and $\varepsilon < 50$ mm/monsoon rather than $\varepsilon > 0$ and $\varepsilon < 0$ to allow for some uncertainty in the computed value of ε due to data errors. In the absence of ground observations on external water imports and river discharge in the studied basin to validate these thresholds, we consider them as reasonable approximations for guiding the combinations of products exclusion process.

3. Monthly gridded water balance data sets

This section describes the water balance data sources and their general characteristics. The data sets are primarily accessed through the Google Earth Engine cloud computing platform or other public repositories. They are categorized into: remote sensing (RS), Ground-Based Measurements (GBM), Water Balance (WB) and Land Surface Models (LSM). All products were resampled to the same spatial resolution using bilinear interpolation for a consistent comparison. Table 2 differentiates between each data set's original and resampled resolutions.

Four gridded precipitation products are selected for evaluation, including the Tropical Rainfall Measuring Mission (TRMM) (Huffman et al., 2007), the NASA/JAXA Global Precipitation Measurement (GPM, IMERG) (Huffman et al., 2019), Climate Hazards Group Infrared Precipitation with Stations (CHIRPS) (Funk et al., 2015), and the Multisource Weighted-Ensemble Precipitation (MSWEP) (Beck et al., 2019). Each of these products merges a variety of ground- and satellite-based observations. Text A.1. and Table A.1. of the Appendix include detailed information on the different data sources and algorithms used to generate the studied precipitation products.

Seven gridded ET products encompassing various ET calculation methodologies are used: pyWaPOR-ET based on the ETLook model (Bastiaanssen et al., 2012) (pyWaPOR v2.6 –authors' generated product named similar to the open-access python package used to generate it), the operational Simplified Surface Energy Balance (SSEBop) developed by the United States Geological Survey (USGS) (Senay et al., 2013), Landsat Collection 2 Provisional Actual Evapotranspiration Science Product (Senay, 2018; Senay et al., 2023), the Surface Energy Balance Algorithm for Land (SEBAL) (Bastiaanssen et al., 1996, 1993; Bastiaanssen, 1995), the Atmosphere-Land Exchange Inverse model (ALEXI) developed by the United States Department of Agriculture (USDA) (Anderson et al., 2007, 2015), the MOD16A2 V6 product supported by NASA Earth Observing System (Mu et al., 2011), and the CSIRO MODIS Reflectance-based Scaling ET model (CMRSET) (Guerschman et al., 2009). Although most of these products use MODIS satellite data as input (ALEXI, CMRSET, SSEBop, pyWaPOR, and MOD16), their ET modeling approaches are markedly different. Both pyWaPOR and MOD16 are Penman-Monteith (PM) ET mapping models. pyWaPOR-ET is based on the ETLook model (Bastiaanssen et al., 2012), which uses two parallel Penman-Monteith (PM) equations for both the canopy and soil to predict transpiration and evaporation. MOD16 is a three-layer PM model driven by RS data from the MODIS sensor and meteorological data from MERRA GMAO. MOD16 partitions ET between transpiration (T), soil evaporation (E), and Interception (I). The SEBAL ET model is a single-source energy balance model representing vegetation and soil in a combined energy balance. ET is calculated as a residual of the energy balance at a spatial resolution of 30 m. Thermal imagery from Landsat imagery is a crucial input to the SEBAL model. We developed a java-script Earth Engine-based implementation of the SEBAL model at 30-m resolution (eeSEBAL) with the ET product named similar to the script in its creation. On the other hand, SSEBop uses a simplified version of the surface energy balance. Like SEBAL, the estimation of ET with SSEBop is based on hot and cold pixels using differences between land surface and air temperature to determine the ET fraction (ratio of ET and ET_0). ET is then calculated as the product of ET fraction and reference ET (ET_0). We have collected and used two SSEBop-ET products. One is based on MODIS Land Surface Temperature, and the other uses the Landsat C2 Level-2 Surface Temperature as input, hereafter referred to as SSEBop (a) and SSEBop (b), respectively. The Landsat Provisional ET product (Landsat-based SSEBop, SSEBop (b)) also uses different inputs: auxiliary data for the temperature difference between hot and cold limits (dT) derived using meteorological data from the European Centre for Medium-Range Weather Forecasts (ECMWF) Reanalysis v5 (ERA5), the maximum air Temperature from the 1981–2010 climatological normal from the CHELSA Version 2 dataset (Thornton et al., 1840), and alfalfa-reference ET (ETr) derived using MERRA-2 which is in turn scaled and corrected via terrestrial ecoregions form OneEarth and scaled Worldclim ET_0(Abatzoglou, 2013; Dinerstein et al., 2017; Hobbins et al., 2022; Li et al., 2019a; Wang et al., 2010; Zomer et al., 2022). In comparison, CMRSET relies on shortwave infrared data to assess vegetation water content as a surrogate of ET fraction. CMRSET uses the Enhanced Vegetation Index (EVI) and Global Vegetation Moisture Indices (GVMI). Both ALEXI and CMRSET use the Priestley-Taylor equation, valid for saturated land surfaces (Priestley and Taylor, 1972), with one distinction: CMRSET utilizes the Priestley-Taylor equation for reference ET, while ALEXI uses it for potential crop transpiration. ALEXI's algorithm is based on a 2-layer surface energy balance (TSEB) model, which separates latent heat flux (λE) into soil and canopy components. Since MOD16 product does not provide ET for non-vegetated grid cells (Running et al., 2017), we masked out these pixels from other ET products for consistent comparisons. All collected and generated ET products are used as provided globally without local calibration. More details on the studied ET products' data sources and theoretical background can be found in the cited references and Text A. 2. of the Appendix.

We also compare soil moisture storage (SMS) data from various sources. The SMS (surface and subsurface) data comparison provides a complementary perspective to the total water balance analysis. We incorporate SMS data from remote sensing, water balance models, and land surface models (LSMs). The limited availability of the SMS from remote sensing compared to the widely available LSM-based SMS motivates a rigorous comparison between the different data sets. The thermal remote sensing SMS from pyWaPOR is derived using a two-step procedure. First, the relative soil moisture (%) is computed based on estimates of maximum temperature at dry conditions, the minimum temperature at wet conditions, and land surface temperature from MODIS using the pywapor script v2.6. Second, the relative soil moisture is converted into actual soil moisture by multiplying it by the subsoil saturated water content (θ_{sat}) (0–100 cm) and the root depth (100 cm). We further use two NASA-USDA Root Zone SMS products: NASA-USDA SMOS and NASA-USDA SMAP products. These products are generated by assimilating SMAP Level 3 soil moisture observations and SMOS Level 2 soil moisture observations into the modified two-layer Palmer model using a 1-D Ensemble Kalman Filter (EnKF) data assimilation approach. The subsurface depth of the two products depends on the depth of the effective root-zone calculated in the two-layer Palmer model (up to 100 cm). Additionally, we incorporate LSM-based SMS data sets from GLDAS driven by the Catchment land surface model (CLSM) (Rodell et al., 2004) and ERA5 driven by Hydrology Tiled ECMWF Scheme for Surface Exchanges over Land (HTESSEL) (Hersbach et al., 2020). GLDAS contains two depth intervals (0–2 cm and 2–100 cm), while ERA5 provides water storages of three soil layers (0–7,7–28, 28–100 cm). We summed the soil moisture across the layers for GLDAS and ERA5 to obtain the total soil moisture per pixel at a monthly timestep. Finally, we include the Terra Climate monthly soil moisture storage data set (at a 4 Km grid resolution) (Abatzoglou et al., 2018). Terra Climate is as an output of a single bucket modified Thornthwaite-Mather climatic water-balance model. The model combines high-spatial resolution climatological normals from the WorldClim dataset with coarser spatial resolution from CRU Ts4.0 and the Japanese 55-year Reanalysis (JRA55) along with extractable soil water storage capacity data from Wang-Erlandsson et al. (2016). Compared to the multi-depth soil moisture data sets used in this study, the Terra Climate SMS product is a single-depth layer. Its depth depends on the spatially variable soil water storage capacity used in the modified Thornthwaite-Mather climatic water-balance model (up to 100 cm).

For the total water storage variable, we use the GRACE Tellus (GRCTellus) Monthly Mass Grids composed of three spherical harmonic data sets produced by three centers: CSR (U. Texas / Center for Space Research), GFZ (GeoForschungsZentrum Potsdam), and JPL (NASA Jet Propulsion Laboratory) (Watkins et al., 2015; Wiese et al., 2016), hereafter referred to as CSR, GFZ, JPL, respectively. We multiply the GRCTellus Land data by the spatially distributed scaling grid to counteract the effects of attenuation induced by sampling and post-processing GRACE observations. We compare these data sets to the GRACE Tellus (GRCTellus) Global Mascon data (Landerer and Swenson, 2012; Swenson and Wahr, 2006). The GRCTellus Mascon data set uses a-priori constraints in space and time to estimate the gravity fields in terms of Mascon functions to minimize the effect of measurement errors and produce better signal-to-noise ratios of the Mascon fields than the conventional spherical-harmonic solutions. We use the version that applies the Coastline Resolution Improvement (CRI) filter to separate the land and ocean contributions to mass changes (Wiese et al., 2016). A linear regression was used to fill the temporal gaps (approximately every 5–6 months) from 2011 onwards. Throughout the paper, we use the abbreviated notation "MAS" to refer to the GRCTellus Mascon data set.

4. Case study: Hindon River Basin in Northern India

The analysis is performed in the Hindon River basin in northwestern Uttar Pradesh (India), see Fig. 1. The Hindon basin is a tributary of the Yamuna River. It joins the Yamuna River at the outlet of the basin near Delhi. The Yamuna River then joins the Ganges at the confluence in Prayagraj, a city in Uttar Pradesh. The Hindon basin covers an area of about 6000 km^2 with a topography that varies from steep in the upper basin to almost flat in the middle and lower parts. The Hindon basin lies in three Koppen-Geiger climatic regions: Monsoon-influenced humid subtropical climate (Cwa), Monsoon-influenced temperate oceanic climate (Cwb) in the middle and upper parts of the basin, and Hot semiarid (Bsh) (lower part of the basin). Relatively little precipitation occurs outside of the June-September monsoon season. Fig. 1. shows the spatial distribution of the long-term average precipitation (2003–2019) derived from a gridded precipitation data set based on gauge observations from the India Meteorological Department (IMD). A clear gradient with declining rainfall amounts moving towards the lower parts of the basin can be observed. The Northern part of the basin receives about 1600 mm/year, while the lower part receives approximately 800 mm/year.

The basin is experiencing several challenges, including a rising population (Bhat, 2014), overexploitation of groundwater resources for irrigation (Rodell et al., 2009), declining streamflow outside the monsoon season (Maheswaran et al., 2016; Mukherjee et al., 2018), and deteriorating water quality (Lewis, 2007). In addition to these challenges, hydro-climatological observations are not easily accessible. The only publicly available data are either provided at a coarse resolution of a district level (such as groundwater pumping) or based on old figures (such as river discharge) (Jain and Sharma, 2006).

Soils in the basin are alluvial deposited by the Hindon River system, with notable proportions of sand and clay characterized by good drainage and soil moisture retaining properties (Sachar, 2015). Soils are fertile for growing three major crops: wheat, sugarcane, and rice (Pingali, 2012). The croplands represent approximately 73 % of the basin, and orchards are also common (~15 %) (Zanaga et al., 2022). Irrigated Croplands cover about 85 % of the basin area (Gumma et al., 2022). An extensive canal irrigation system (Upper Ganga Canal; UGC; and Eastern Yamuna Canal; EYC) exists in the basin to convey water during non-monsoon (dry) and monsoon (rainy) seasons. Water is diverted through the canal system from external reservoirs outside the basin (i.e., Hathni Kund on the Yamuna River and Bhimgoda reservoir on the Ganga River).

Given the above-described basin characteristics, the prevailing water management practices, and the complex water management challenges, the Hindon Basin offers an invaluable testing bed for our proposed methodology. The implementation in the small-sized Hindon Basin pushes the limits of hydrological remote sensing applications to the scale at which most practical water management decisions are often made. The studied basin provides a representative example of many other basins worldwide, often facing similar issues, such as the poor availability of observational networks.

5. Results and discussion

We first present results for each variable individually (P, ET, water storage) in Sections 5.1–5.3, followed by assessing the overall water balance in Section 5.4.

5.1. Precipitation (P)

The monthly precipitation estimates from all products consistently peak in July and reach their lowest in the post-monsoon (Oct-Dec) and pre-monsoon seasons (Jan-May) (Fig. 2. a). In general, all products show the same seasonal trend. GPM and MSWEP values are higher than CHIRPS values during the monsoon season (June, July, and Aug), while TRMM values are the lowest. TRMM exhibits the lowest triple collocation error (13 mm/month), followed by MSWEP (16.5 mm/month), while CHIRPS displays the highest error (50.8 mm/month) (Fig. 2. b) (spatial distributions of TC errors are presented in Fig. A.1).

Differences across the data sets are also apparent at an annual timescale. CHIRPS explicitly shows a broader range from 480 to

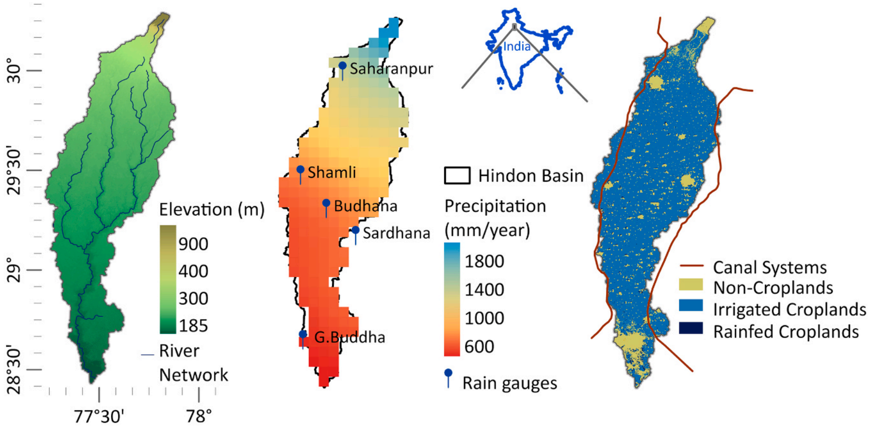

Fig. 1. Hindon River basin: (left) A topographic map with the basin's boundary derived from the HydroBASINS product (Lehner et al., 2008), (middle) India Meteorological Department (IMD) annual precipitation (mm/year) averaged for 2003–2019 and resampled to 0.05° along with locations of the available rain gauges, (right) distribution of rainfed and irrigated cropland areas in the basin from Gumma et al. (2022).

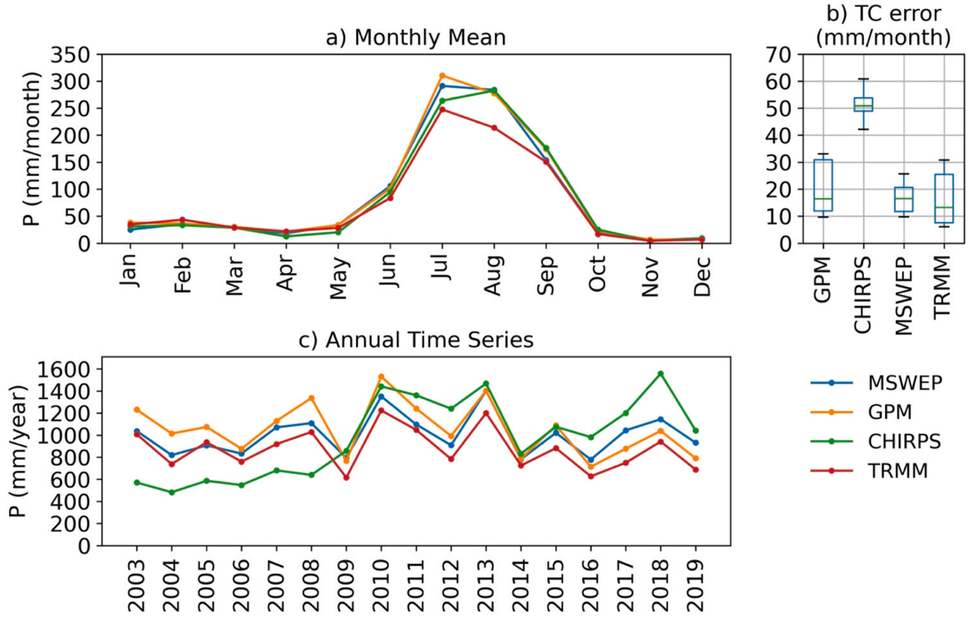

Fig. 2. Comparison of data sets describing the P variable in the Hindon basin, the top panel from left to right depicts a) monthly mean P (all values are in mm/month), b) boxplots showing the triple collocation errors (mm/month), and the bottom panel shows c) annual P time series (all values are in mm/year).

1558 mm/year. Besides, CHIRPS exhibits variability over the years, with lower values observed before 2010 and higher P estimates than the other data sets afterward (Fig. 2. c). All products maintain a long-term annual P estimate close to 1000 mm/year, except for TRMM, which shows a lower estimate of approximately 875 mm/year.

The variations across P data sets are linked to different retrieval methods, data sources, estimation procedures (Sun et al., 2018), rain-gauges network density, differences in spatial resolutions (Maggioni and Massari, 2018), and the basin's climatic characteristics. The grid-scale inter-product uncertainty represented by the CV (%) of the annual P maps shows that uncertainties from the P products tend to be the highest in the areas with lower precipitation in the basin's hot semiarid climatic region (Fig. 3). This finding is expected and aligns with other studies showing a decrease in the correlation of different P products in arid regions with lower rainfall (Awange et al., 2016). Some satellite sensors, such as CHIRPS, largely rely on IR techniques that might be less sensitive to semi-arid regions' lower, highly variable, and infrequent precipitation characteristics or the flat topography characterizing the Hindon basin (lack of orographic rains). Also, shallow or non-precipitating clouds might influence the IR signal. However, incorporating microwave observations benefits the other products (TRMM and GPM IMERG), which are better than the IR techniques due to the more direct observation of precipitation particles' scattering and microwave radiation emission (Kidd and Levizzani, 2011). The density of the rain-gauges network is another factor contributing to the high grid-scale inter-product uncertainty. For instance, CHIRPS differs significantly from the other products as it incorporates climatology data (CHPclim) constructed using sparse gauge stations. Consequently, CHIRPS loses accuracy where the gauge density network is low (the case of the Hindon basin). On the contrary, MSWEP assigns weights to gauge-based estimates based on the gauge network density, thus accounting for the presence of few gauges in the basin.

A significant spatio-temporal consistency exists between the P products at both long-term annual and monthly timescales, with an R^2 above 0.8. The highest spatial consistency of the mean annual precipitation is found between TRMM and MSWEP (R^2=0.98), followed by the consistency between TRMM and GPM (R^2=0.96) (Fig. 4). The highest consistency in the TRMM-MSWEP pair can be

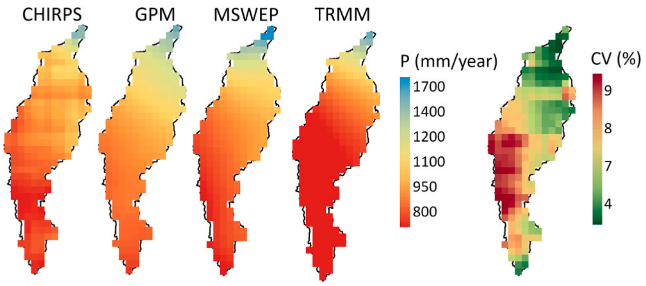

Fig. 3. Long-term mean annual P spatial maps (2003–2019) for each product and the corresponding variability across all products expressed as CV.

attributed to the fact that MSWEP is a merged product, which, therefore, has accounted for uncertainties from different data sources; besides, it uses TMPA as a data source in the merging process. TRMM-GPM's high consistency is related to the TMPA product providing P estimates using data from GPM after TRMM's mission ended in 2015. Another aspect is that the GPM satellite was launched in 2015, but the IMERG product starts in 2000 using TRMM data. The consistency between GPM and TRMM is also explained in other studies, showing that both products exhibited high correlation and similar spatial patterns in most of the studied basins in India (Beria et al., 2017).

Conversely, the assessment based on the long-term monthly precipitation suggests that the TRMM-GPM combination showed the highest spatio-temporal consistency throughout the whole seasonal cycle, but MSWEP-TRMM showed a stronger spatio-temporal consistency during the rainy season (June-Sept). In contrast, CHIRPS is highly inconsistent with all P combinations (specifically in pre-and-post-monsoon season). In general, TRMM is more comparable to other products.

Precipitation products are evaluated against rain gauge observations based on their statistical behavior over the entire time series (Fig. 5). The highest RMSE values are shown in months with the highest precipitation estimates (i.e., monsoon season). In contrast, the highest pBIAS (%) was found in months with the lowest precipitation estimates (April and January). Overall, TRMM showed an adequate agreement with the in-situ observations. Despite its high resolution compared to other products (allowing it to detect local variations), CHIRPS exhibited the highest RMSE values (ranging between 85 and 185 mm/month) and lowest correlation ($r \leq 0.35$) with the rain gauge data during the rainy season, demonstrating an inadequate agreement with the in-situ observations. This suggests that CHIRPS resolution is not the sole factor affecting its uncertainty, and other factors, such as the data sources (ground and satellite observation) and the satellite retrieval algorithm, have a more pronounced influence. Overall, this evaluation and the consistency and uncertainty analysis results conclude the exclusion of CHIRPS from further analysis.

5.2. Evapotranspiration (ET)

The long-term seasonal cycle of ET shows that MOD16 had the lowest ET values in all months, particularly in the pre-monsoon period, indicating its inability to capture the ET dynamics of irrigated crops (Fig. 6. a). MOD16-ET forms an unusual dip in April-June (close to zero). MOD16 tendency to underestimate ET in irrigated croplands was also indicated in previous studies (Mu et al., 2011; Velpuri et al., 2013). On the other hand, MODIS-based SSEBop (SSEBop(a)) showed the highest ET values between May and Sept. eeSEBAL, and MODIS-based SSEBop (SSEBop(a)) showed higher ET values than the other products in the pre-monsoon period (Feb-May), where conjunctive irrigation practices (both surface and groundwater pumping) are prevalent; however, MODIS-based SSEBop (SSEBop(a)) showed higher estimates than eeSEBAL. This aligns with other studies conducted in irrigated areas of the High Mountain Asia region, showing that (SSEBop(a)) produced very high ET estimates (De Kok et al., 2020). During the monsoon period (from July to Sept), the ET rates have dropped in all models except MOD16 and CMRSET. During the post-monsoon (Oct-Dec), ET rates decreased in all products except eeSEBAL. The Simplified Surface Energy Balance (SSEBop) model, fed by different inputs, provides remarkable differences in ET seasonal cycles, with Landsat-based SSEBop (SSEBop(b)) showing lower ET estimates compared to the MODIS-based SSEBop (SSEBop(a)) output, which overestimates ET. To clarify, the temperature difference (dT) data set of the Landsat-based SSEBop model is determined using net radiation inputs under gray-sky conditions incorporated from the high-resolution ERA5 reanalysis data, which accounts for the effect of clouds on the incoming solar radiation and improves the estimation of ET fraction, especially in the cloudy monsoon season. On the other hand, the MODIS-based ET (SSEBop(a)) assumes clear-sky conditions

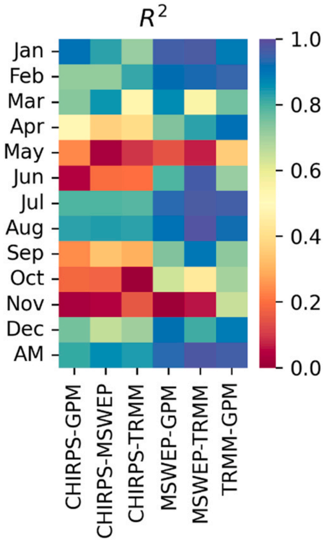

Fig. 4. Pair-wise pixel-by-pixel spatio-temporal consistency among the evaluated P products at two-time shots: mean monthly P and long-term annual P means. AM is an abbreviation for Annual Mean.

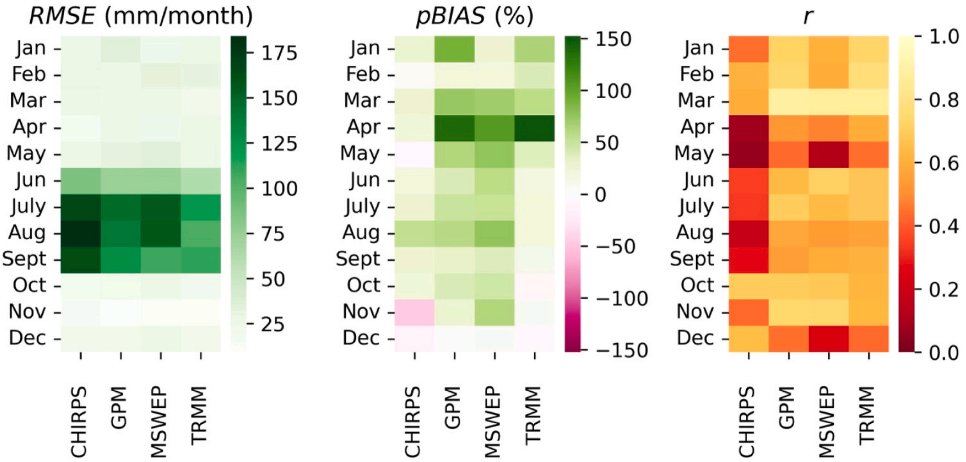

Fig. 5. Heat maps of statistical performances of different precipitation products against rain gauge observations using point-to-grid comparison at a monthly timestep. RMSE values are in mm/month.

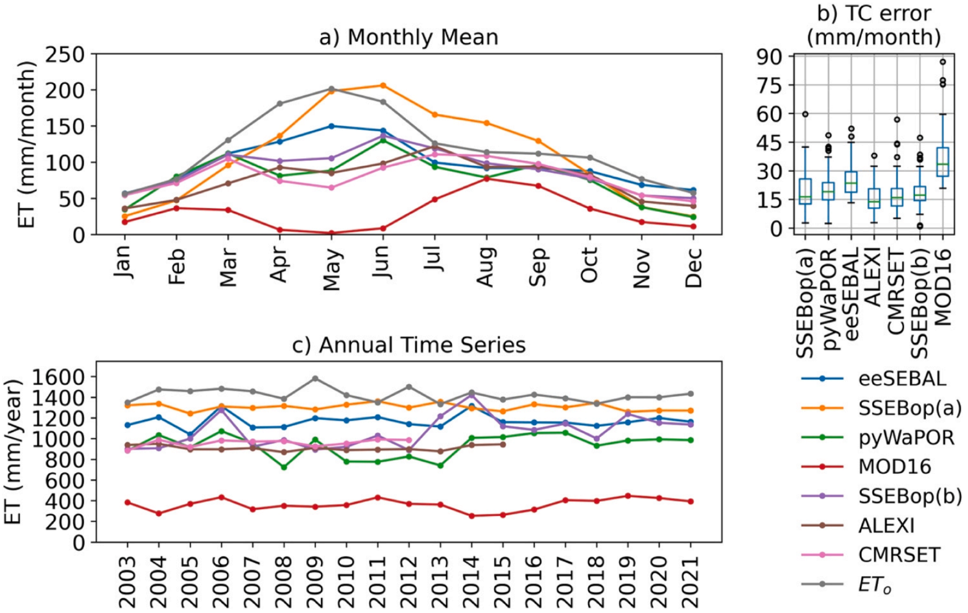

Fig. 6. Comparison of data sets describing the ET variable in the Hindon basin: the top panel from left to right depicts a) monthly mean ET(all values are in mm/month), b) boxplots showing the triple collocation errors (mm/month), the bottom panel shows c) annual ET time series (all values are in mm/year). SSEBop(a) and SSEBop(b) represent MODIS-based and Landsat-based SSEBop products, respectively.

in the net radiation calculations. A further noteworthy feature is that MODIS-SSEBop's capacity to capture detailed weather variables is limited since it computes ET_0 using meteorological data sets from coarser reanalysis products: Global Data Assimilation System (GDAS). Additionally, MODIS-SSEBop (SSEBop(a)) coarse resolution (1 Km) limits its ability to capture subpixel variability caused by surface heterogeneity and highly variable soil moisture dynamics, especially in the monsoon season with intermittent precipitation and surface-water irrigation practices.

The timing of the peaks also differs across the products. Some ET models show one peak, while others show two peaks. eeSEBAL and MODIS-based SSEBop have one peak in May and June, respectively. In comparison, pyWaPOR, ALEXI, CMRSET, MOD16, and Landsat-based SSEBop have two peaks in March-June, March-July, April-July, and March-Sept, March-June, respectively. A noteworthy feature is that ALEXI's peak in the rainy season is higher in magnitude than in the dry season. In contrast, the two peaks of CMRSET ET are close in magnitude in dry and monsoon (rainy) seasons.

Comparisons against the ET_0 show that all ET models exhibit lower values than ET_0, except that the MODIS-based SSEBop (SSEBop (a)) model generates higher estimates than ET_0 during the monsoon season. In contrast, MOD16 negatively correlates with ET_0 throughout the seasonal cycle and falls far below ET_0, an uncommon pattern. ALEXI, pyWaPOR, CMRSET, and Landsat-based SSEBop correlate poorly with ET_0 between April and June.

The TC error analysis shows that the mean error in the different data sources ranges between 15 and 38 mm. ALEXI showed the lowest error as it correlates well with all products (r ranging between 0.5 and 0.7). The highest mean error corresponds to the MOD16 (38 mm/month) followed by eeSEBAL (26 mm/month) (spatial distributions of TC errors are presented in Fig. A.2). eeSEBAL showed a high error due to the significant difference in magnitude and peak timing compared to the other ET models (Fig. 6. b).

ET models also show high variability in magnitudes at an annual scale (Fig. 6. c). MOD16 ET represents the lowest range with values close to 360 mm/year. pyWaPOR, ALEXI, CMRSET, and Landsat-based SSEBop have similar annual ET ranges with values close to 900–950 mm/year. However, SSEBop(a) shows the highest ET values, approximately 1300 mm/year, followed by eeSEBAL, approximately 1150 mm/year. Landsat-based SSEBop (SSEBop (b)) shows higher ET estimates from 2012 onwards than in previous years, closer to eeSEBAL ET estimates. This overlaps with the period when Landsat observations became more frequent with the launch of Landsat 8 in 2013.

The ET products show unexpected, widely diverging spatial patterns (Fig. 7). Apart from different spatial resolutions, several other factors may have caused these variations, as discussed in the following lines focusing on high-resolution ET estimates (Fig. 7). The grid-scale inter-product uncertainty is higher in areas of the urban and non-vegetated land use class. This can be linked to the differences of the ET models in handling these landcover classes. pyWaPOR ET, for instance, uses land use classes from GlobCover to assign values for the roughness length of momentum ($z_{0,m}$), which is used in calculating the aerodynamic resistance (r_a) of the different surfaces. The lower ET estimates from pyWaPOR ET are consistent with the expected reduced ET over urban surfaces from other vegetated areas compared to other models (e.g., eeSEBAL) showing higher ET estimates over the urban classes. Improving ET estimates in heterogeneous urban surfaces has been the focus of a few studies (e.g., (Faridatul et al., 2020)). CV is also high over the irrigated land (>20 %). The high uncertainties in irrigated cropland further suggest that the ET models have varying and contrasting sensitivities to soil moisture dynamics (altered by precipitation and conjunctive irrigation practices) and water-limited conditions (in a dry season). ET modeling approaches differ in representing these conditions. To capture the impact of precipitation on ET via interception losses, pyWaPOR-ET, for example, relies on CHIRPS precipitation data as a key input variable. However, CHIRPS was identified as an unreliable data set over the studied basin (Section 5.1). On the other hand, ET models do not explicitly consider the soil moisture dependency when calculating ET, and some assume that it is implicitly incorporated in the land surface temperature (LST) variable. This assumption is adequate when the available energy is a limiting factor for ET but not when water availability becomes a limiting factor (Gokmen et al., 2012). For example, the energy balance models or simplified energy balance models, such as eeSEBAL and SSEBop (b) incorporate soil moisture influence in the ET fraction, which is determined as a function of LST and other inter-relatable variables, while in pyWaPOR-ET, relative soil moisture is derived as a function of LST and other variables (e.g., vegetation cover) used as a soil moisture proxy which is also used to calculate soil moisture stress. For the studied basin, the intermittent rainfall events in a monsoon season can create temporal water-limited conditions necessitating supplemental irrigation (Kishore et al., 2023). However, pyWaPOR soil moisture showed a muted response to increased soil moisture conditions caused by the combined rainfall and irrigation events during the monsoon season (see Section 5.3.1). Also, anthropogenic factors caused by irrigation water source (surface vs. groundwater), application method and timings, and efficiency (flood, drip) introduce heterogeneity in the irrigated crop surfaces and can highly influence the ET dynamics. Most ET models do not explicitly consider these human elements, causing high inter-model discrepancies.

The pixel-to-pixel spatial consistency of the long-term annual ET depicts a significant spatial inconsistency between the products with an R^2 not higher than 0.75. The highest spatial consistency of the mean annual ET is between eeSEBAL and pyWaPOR (R^2=0.69), followed by pyWaPOR-Landsat-based SSEBop (R^2=0.55) and eeSEBAL-Landsat-based SSEBop (R^2=0.52). The monthly spatio-temporal analysis shows that MODIS-based SSEBop ET exhibited the poorest correlation with all ET products in space and time. The strongest relations are found between the pairs: eeSEBAL-pyWaPOR, pyWaPOR-Landsat-based SSEBop, and eeSEBAL-Landsat-based SSEBop throughout the seasonal cycle except for a few months (Fig. 8).

The combined results of TC and spatio-temporal analysis foster the exclusion of MOD16 as it shows the highest TC error, falls far below the ET_0, and fails to capture the ET of irrigated croplands in both space and time.

Comparisons of RS-ET models continue to show significant variations due to differences in modeling strategies and assumptions. To

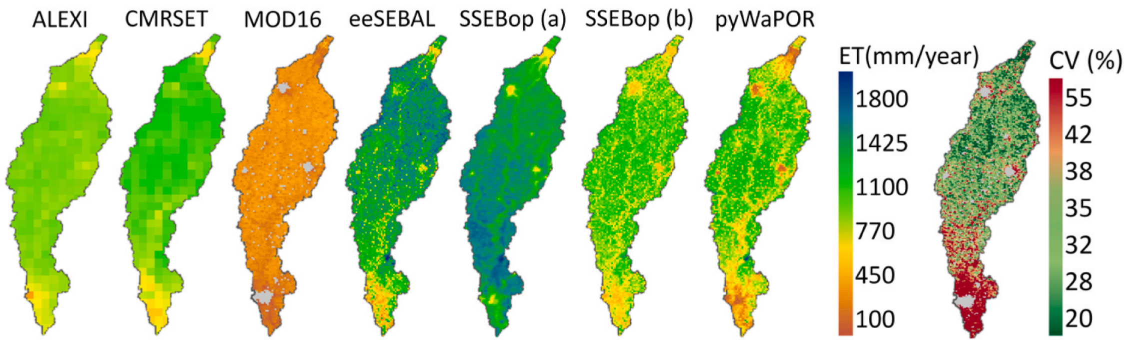

Fig. 7. Long-term mean annual ET spatial maps (2003–2012) for each product and the corresponding grid-scale variability among the products expressed as a Coefficient of Variation. SSEBop (a) and SSEBop (b) represent MODIS-based and Landsat-based SSEBop products, respectively.

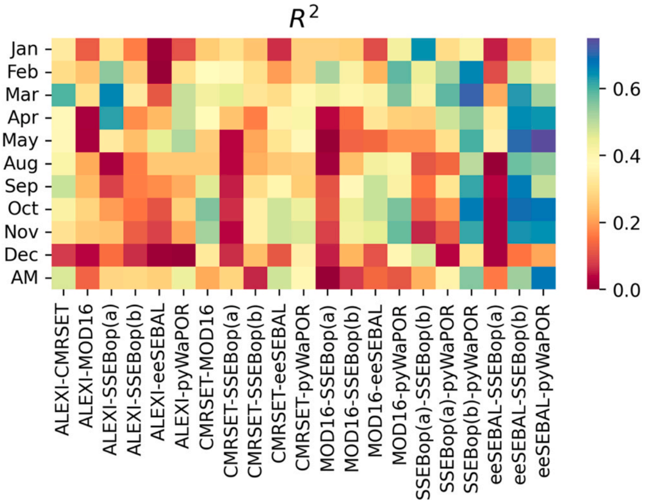

Fig. 8. Pair-wise pixel-by-pixel spatio-temporal consistency among the evaluated ET products at two-time shots: mean monthly ET and long-term annual ET means. AM is the abbreviation for annual mean. SSEBop (a) and SSEBop (b) represent MODIS-based and Landsat-based SSEBop products, respectively.

clarify, the eeSEBAL model treats the energy balance for the canopy and soil in a combined manner, thus exhibiting biases in partially vegetated cover. In contrast, ALEXI assumes an initial and universal Priestley-Taylor (P-T) coefficient for all landscapes and climates, which is unlikely unless locally adjusted. The accuracy of the SSEBop model relies on its constant parameters, such as the k coefficient used to scale the grass reference ET and the aerodynamic resistance to heat flow (r_{ah}), which limits its regional application as it requires local calibration and parameterization. Additionally, all ET model's accuracy relies on the accurate estimation of aerodynamic and surface and canopy resistances (Li et al., 2019c), which remains a challenging task to quantify temporally due to changes in atmospheric forcing and spatially due to landscape heterogeneity (Evans et al., 2012).

Inputs to these models also form another source of variation. For instance, MOD16 requires accurate land cover classification as an input for the parametrization of biome properties (Kim et al., 2012; Kiptala et al., 2013). All the above models are based on reference ET, each with a particular form of the PM equation (FAO standard version or Priestley-Taylor). Therefore, the uncertainties in all models are related to the quality of meteorological inputs (Li et al., 2019b; Yang et al., 2015). The LST-based models (ALEXI, SSEBop, pyWaPOR, and eeSEBAL) are more sensitive to LST accuracy (Biggs et al., 2016). For instance, ALEXI becomes more sensitive to LST in

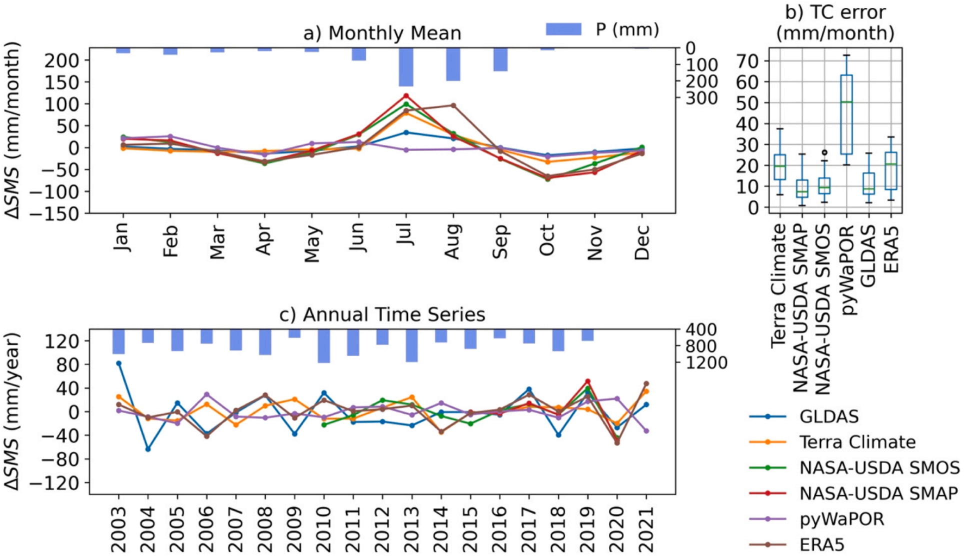

Fig. 9. Comparison of data sets describing the ΔSMS variable in the Hindon basin: the top panel from left to right depicts a) monthly mean ΔSMS and monthly mean TRMM P plotted as bars (all values are in mm/month), b) boxplots showing the triple collocation errors (mm/month), the bottom panel shows: c) annual ΔSMS time series and annual mean TRMM P plotted as bars (all values are in mm/year). All ΔSMS products are for the root zone.

conditions of full canopy coverage, causing uncertainties in soil and canopy temperature partitioning (Kustas and Anderson, 2009). The variations in terms of inputs (land surface temperature and meteorological data) are evident when comparing estimates from MODIS-based SSEBop (high) to that of Landsat-based SSEBop (low).

Other factors, such as cloud cover, form a severe problem in humid areas, like the Hindon basin, where clouds can highly impact the LST-based models, leading to lower ET due to lower incident radiation, thus impacting ET accuracy (Jiang et al., 2018). As applied in the eeSEBAL, Landsat-based SSEBop (b), and pyWaPOR, gap-filling techniques might also introduce uncertainties in ET estimates if the gap between the ET scenes is very long or the ET ratio is not conservative (Ma et al., 2018).

5.3. Water storage change

5.3.1. ΔSMS

The NASA-USDA SMAP and SMOS ΔSMS root zone soil moisture data sets showed a consistent seasonality (Fig. 9. a). The ΔSMS from NASA-USDA SMOS and SMAP, Terra Climate, and GLDAS data sets peaked in July, indicating a gain in soil water storage; however, NASA-USDA SMOS and SMAP detected a higher peak ΔSMS magnitude than GLDAS and Terra Climate. pyWaPOR ΔSMS product showed an inconsistent seasonality with other products, indicating an unexpected loss of soil water storage during a rainy season (between June and August). pyWaPOR v2.6 estimates relative soil moisture within the LST-NDVI space using a trapezoidal method. This approach, however, is sensitive to the correct estimation of the trapezoid's corner points that are hard to establish during a cloudy and rainy season (Wang et al., 2010). pyWaPOR becomes more consistent with Terra Climate and GLDAS in April and Oct (with less vegetation cover). In contrast, changes in soil moisture storage from ERA5 peaked in August. Collectively, the land surface models (GLDAS and Terra Climate) captured larger magnitude fluctuations than NASA-USDA SMAP and SMOS products for the period extending from Sept to Dec.

GLDAS and Terra Climate ΔSMS are consistent with NASA-USDA SMOS and SMAP ΔSMS ($r= 0.9$ and 0.8, respectively). The good agreement between Terra Climate and the root zone soil moisture products derived from SMOS and SMAP could be attributed to its relatively high resolution (4Km), which incorporates spatially distributed root zone storage capacity data from Wang-Erlandsson et al. (2016), potentially capturing the impacts of spatial heterogeneity and the variability in the root zone storage capacity within land covers. Along with other variables, the root zone storage capacity in Terra Climate is derived from the ensemble mean of evaporation data (e.g., SSEBop and CMRSET), thus implicitly accounting for irrigation. On the other hand, GLDAS assimilates total water storage from GRACE capturing broad-scale water storage dynamics (Li et al., 2019a). The TC findings indicate comparable errors between NASA-USDA SMAP (9.6 mm/month), NASA-USDA SMOS (11 mm/month), and GLDAS (11.6 mm/month) ΔSMS data sets, while pyWaPOR revealed the highest error (44.4 mm/month) (Fig. 9.b). Terra Climate (19 mm/month) and ERA5 (18.5 mm/month) ΔSMS errors lie between the other data sets' errors.

Comparisons against the precipitation pattern indicate that ERA5 ΔSMS exhibits a shift/lag in its time series, which peaks one month after the peak rainy month. Tuinenburg and de Vries (2017) showed that the ERA5-soil moisture additions strongly correlate with irrigated areas of the Ganges River Basin (encompassing the Hindon Basin as a subbasin), but there is a bias in ERA5 precipitation. The variations across the ΔSMS data sets are less at the long-term annual temporal scale (Fig. 9.c), with Terra Climate, ERA5, and NASA-USDA SMAP ΔSMS products exhibiting small gains in long-term mean annual ΔSMS of 1.14, 1.55, and 1.21 mm/year, respectively, while NASA-USDA SMOS, pyWaPOR, and GLDAS ΔSMS displayed small losses in the long-term mean of −1.78, −0.52, and −1.76 mm/year, respectively.

The ΔSMS data sets also provide divergent spatial patterns throughout the seasonal water cycle, particularly during the monsoon season. We here showcase the month of July (peak rainy month), capturing the spatial patterns and variability between the products (Fig. 10). The grid-scale inter-product uncertainty tends to be the highest in the middle part of the basin, where pyWaPOR showed an unexpected loss compared to other data sets showing a gain in storage except that GLDAS shows a slight gain. In contrast, Terra Climate displayed a higher magnitude gain in storage in the upper part of the basin than the other products (ERA5, NASA-USDA SMAP and

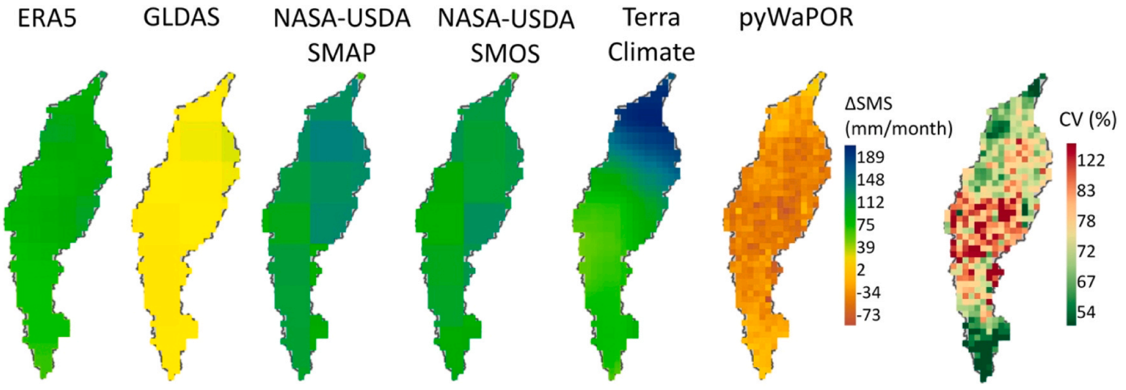

Fig. 10. Long-term mean ΔSMS spatial maps for July (2016–2020) for each product and the corresponding grid-scale variability among the products expressed as a Coefficient of Variation. All ΔSMS products are for the root zone.

SMOS). Terra Climate product resembles the precipitation gradient across the basin (see Fig. 1, middle panel). The differences in the spatial resolutions, rootzone variability, irrigation practices (e.g., timing, amount, and methods of applications), the products' intrinsic uncertainties, and the forcing input data used to estimate the root zone ΔSMS may have contributed to these diverging responses between the ΔSMS products. USDA-NASA root zone data sets benefit from the assimilation of surface soil moisture (with high temporal resolution) from microwave measurements that can improve the subsurface soil moisture estimates (Bolten and Crow, 2012; Bolten et al., 2009a, 2009b; Han et al., 2014), albeit their coarse spatial resolution. In addition, factors such as precipitation, surface roughness, and vegetation density influence microwave observations (De Jeu et al., 2008; Dorigo et al., 2010). On the other hand, LSMs treat soil moisture as a dynamic parameter, enabling interactions between surface and subsurface. However, these interactions might not be very well captured due to their coarse resolution (Wood et al., 2011) and the incorporation of a simplified representation of subsurface dynamics (Niu et al., 2011). In contrast, cloud cover obscures LST-based soil moisture observations (less data) (e.g., pyWaPOR) (Qin et al., 2013). Additionally, the quality of the LST and the meteorological inputs used to derive the relative soil moisture in pyWaPOR v2.6 might contribute to its unexpected diverging responses compared to the other products. Understanding and quantifying grid-scale inter-product variability and temporal uncertainties in ΔSMS is essential for accurately representing the soil moisture dynamics in water balance analyses.

5.3.2. *ΔTWS*

Estimates of total water storage changes between different GRACE solutions show fewer variations than those between ET and ΔSMS products (Fig. 11. a). Unsurprisingly, the spread within CSR, GFZ, and JPL is small (Michailovsky et al., 2023) compared to the difference against the GRCTellus Mascon (MAS) data set. This aligns with prior analysis of TWS showing greater signal from mascons than gridded SH data sets in ground water-depleted regions in India (Save et al., 2016). The GRCTellus Mascon (MAS) solution has a higher amplitude in Feb, April, and August than the other products. Generally, all solutions indicate a gain in storage during the monsoon season (June-Aug) and a storage loss during post-monsoon (Sept-Dec). The GRCTellus Mascon (MAS) data set shows more storage loss than the other three products in Oct-Dec. The JPL-GFZ and CSR-GFZ pairs also show poor correlations in dry months (Jan, Nov, and Dec). Generally, the CSR-JPL combination shows better agreement throughout the seasonal cycle.

The CSR product is more comparable to the other products (r between 0.7 and 0.9). The MAS product had the lowest correlation with the other three products (r=0.7). This correlation outcome has been reflected in the TC results, showing that the MAS had the highest error (50 mm/month), but CSR exhibited the lowest error (20 mm/month). JPL and GFZ depicted analogous errors (approximately 28 mm/month) (Fig. 11. c).

In terms of the trend in the annualized total water storage anomaly (TWSa), all products showed negative depleting trends indicating regional groundwater overexploitation of varying magnitudes in the range of –31 and –34 mm/year from the three spherical harmonic data sets and –61 mm/year from the MAS solution, with years such as 2004 and 2009 accelerating the process of depletion (Fig. 11. b), qualitatively reflecting previously reported independent information on the groundwater depletion in the basin (Alam and Umar, 2013). In the current study, we applied scaling factors to SH, which helped restore the GRACE signal lost due to truncation and improve the agreement between mascon and SH solutions. We note that the coarse spatial resolution of GRACE in small-sized basins, such as the Hindon Basin, limits its spatial interpretation. However, for consistency and completeness, we show long-term mean annual

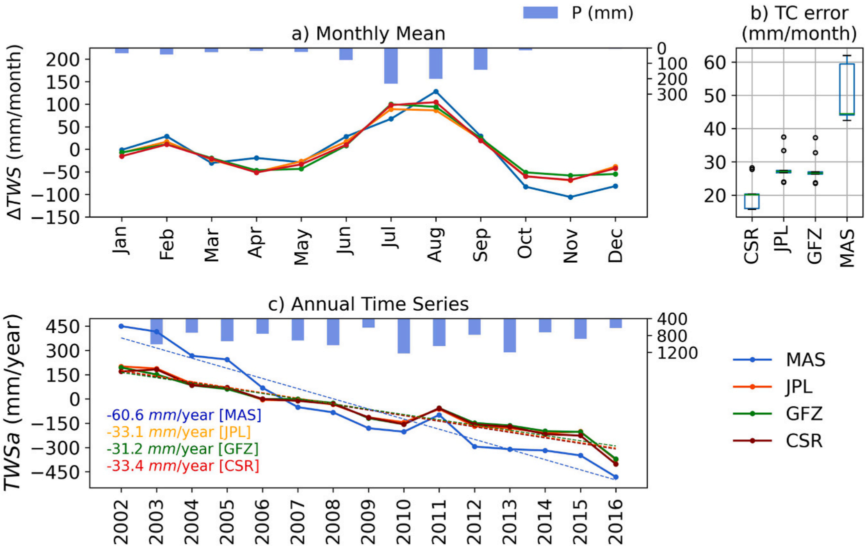

Fig. 11. Comparison of data sets describing the ΔTWS variable in the Hindon basin, the top panel from left to right depicts a) monthly mean ΔTWS (total water storage anomaly converted into monthly rates) and monthly mean TRMM P plotted as bars (all values are in mm/month), b) boxplots showing the triple collocation errors (mm/month), the bottom panel shows: c) annual total water storage anomaly (TWSa) timeseries (TWS changes represented as anomalies relative to long-term mean) and annual mean TRMM P plotted as bars (all values are in mm/year).

ΔTWS spatial maps (2002–2016) in Figure A.4. The figure suggests a moderate mean annual grid-scale inter-product uncertainty (15–19 %).

TWS available from GRACE observations in the form of spherical Harmonic (SH) inherent a range of errors, including noise in the measurements and degree-order truncation of SH coefficients, where noise increases with higher SH degrees corresponding to higher spatial resolution or smaller basins (Chen et al., 2004), striping errors due to unwanted correlation (Swenson and Wahr, 2006), filtering processes to reduce the noise in the SH coefficients (smoothing), which can induce the mutual signal leakage (Swenson and Wahr, 2002). On the other hand, the regional mass concentration (MAS) product is less reliable in small basins due to its coarse spatial resolution (Vishwakarma et al., 2018; Wahr et al., 1998) and the increase of noise signal in smaller mascon blocks (Li et al., 2019a). Other possible sources of GRACE error include the scaling factor obtained from land surface models. Compared to dry and semi-arid regions, Long et al. (2015) demonstrated that the scaling factor's impact may be smaller in humid subtropical climates, such as the case of the Hindon basin. However, because they depend on data from a land surface or hydrological model, the model-derived gain factors –also known as scale factors– are prone to errors, although they enhance the spatial resolution of the GRACE observations and restore the amplitude of the TWS signal. These models may be biased in the conjunctively surface and groundwater-irrigated Hindon basin as they typically do not include groundwater or human activities in their simulations. Long et al. (2015) have also examined the impact of temporal variability of scaling factors and found it to be minor at a basin scale in humid subtropical climates. Another potential source of errors in GRACE TWS is data gaps, which impact trend estimates. The gap-filling methods, such as the linear regression employed in this study, can introduce additional uncertainties to the estimated TWS changes and trends, especially if the missing data are for an extended period.

An intriguing approach to downscale GRACE while limiting the interference of hydrological models is to employ the data error model put forward by Schoups and Nasseri (2021), which yielded encouraging results in semi-arid basins. To account for any variations in the amplitudes and phases between the GRACE storage and the unknown "true" storage caused by "leakage", their model relates the GRACE observations with its underlying true values using the unknown time-invariant error parameters: amplitude (A) and phase difference (δ), which are inferred from all the water balance data. This approach, however, requires data on river discharge out of the basin and irrigation imports and will be the focus of a follow-up study.

5.4. *Reducing prior uncertainties using the seasonal water balance*

In this section, an ensemble of long-term average $Q_{in} - Q_{out} \approx \Delta TWS - P + ET = \varepsilon$ (Eq. 2) is disaggregated per season and solved for unique P, ET, and ΔTWS combinations when available (2003–2012). We report the final (ε) (in mm/season) as the range and mean across all possible combinations (Table 3). When no data sets are excluded (scenario 1), we find a wide range in computed ε, with potentially unrealistic values (negative resp. positive) in non-monsoon and monsoon seasons. Since previous sections suggested that

Table 3

Total P, ET, and ΔTWS per season averaged across the years (2003–2012), with the range and average $\varepsilon \approx Q_{in} - Q_{out}$ before exclusions, after excluding all combinations containing CHIRPS and MOD16-ET, and after applying seasonal constraints on ε. SSEBop(a) and SSEBop(b) represent MODIS-based and Landsat-based SSEBop products, respectively. The applied thresholds per season led to excluding SSEBop(a) from the rainy season when combined with all P and ΔTWS data sets.

		Non-monsoon season (Oct-May)	Monsoon season (June-Sept)
P (mm)	CHIRPS	125	716
	GPM	186	934
	MSWEP	138	855
	TRMM	165	741
ET (mm)	ALEXI	496	394
	CMRSET	545	401
	MOD16	153	208
	eeSEBAL	755	387
	SSEBop(a)	656	633
	SSEBop(b)	560	368
	pyWaPOR	522	361
ΔTWS (mm)	JPL	−288	255
	CSR	−310	283
	GFZ	−295	280
	MAS	−348	278
ε (mm)	Min	−380	−470
(Before exclusion)	Max	342	200
	Average	61	−152
ε (mm)	Min	−38	−318
(After excluding all combinations	Max	330	−174
containing CHIRPS and MOD16-ET)	Average	116	−71
ε (mm)	Min	−38	−318
(After applying soft constraints	Max	330	−57
per season)	Average	116	−187

CHIRPS and MOD16-ET should be excluded, we then evaluate how excluding all combinations containing CHIRPS and MOD16-ET data sets affects the seasonal water balances (scenario 2). Table 3 shows that these exclusions indeed result in more realistic ε values (less negative minimum value in non-monsoon, slightly less positive maximum value in monsoon), validating the exclusion decisions made in previous sections. Finally, for the third scenario, we evaluated which other data sets would need to be excluded to satisfy prior constraints on the seasonal values of ε, i.e., $\varepsilon > -50$ mm (non-monsoon) and $\varepsilon < 50$ mm (monsoon). Applying these constraints further narrowed the ε range between −318 and −57 mm in the monsoon season by excluding the MODIS-based SSEBop model from the monsoon (rainy) season when it appeared in combination with all P and ΔTWS data sets. These constraints allowed for obtaining updated prior estimates of the seasonal water balances by excluding the most significant inconsistent combinations; however, it is essential to note that the choice of thresholds (i.e., strict or relaxed) plays a crucial role in identifying which combinations to exclude and to what extent it is possible to physically constrain the seasonal ε ranges. For the Hindon basin, with the absence of ground-observations data on irrigation water imports and river discharge and the remaining uncertainties associated with the un-excluded data sets, particularly in the non-monsoon season, the applied thresholds did not completely constrain the seasonal ε ranges.

Exclusions of unreliable P (CHIRPS) and ET (MOD16) from the whole seasonal cycle show a significant decrease in the upper limit of triple collocation errors (mm/month) range in individual products by 56 % for P and 39 % for ET (Table 4).

6. Conclusions and future outlook

Many satellite remote sensing data and models provide estimates of water balance fluxes (P and ET) and storages (SMS and TWS) and cover a wide spatial extent, and temporal scales are becoming more easily accessible. However, these estimates are based on different algorithms, parametrization schemes, inputs, and scales and, thus, are hydrologically inconsistent. These products have been validated in their generating processes but are not necessarily accurate for hydro-environmental conditions elsewhere. The current study presents a prior uncertainty analysis for major water balance data sets. The analysis is applied to the Hindon basin, an understudied basin due to limited international data sharing despite its various pressing water management challenges, including groundwater overexploitation and water quality deterioration related to unsustainable irrigation practices.

The uncertainty analysis suggests that P and ΔTWS exhibited consistent seasonality among the water balance components during the rainy season, but ET and ΔSMS displayed greater variations between data sets across the entire seasonal cycle. The P fluxes exhibited fewer spatio-temporal variations (R^2 above 0.8) than ET fluxes (R^2 less than 0.75), with certain combinations having higher consistency than others. Additionally, RS-ET is a highly uncertain flux among the other water balance components due to differences in the evaporation process parametrization with a challenging application in an intensively irrigated basin characterized by a complex seasonality (water limitation necessitating supplemental surface and groundwater irrigation in the dry season and energy limitation and intermittent precipitation during the monsoon season). The grid-scale inter-product uncertainty analysis shows a moderate mean annual inter-product variability for P (5–9 %) and ΔTWS (15–19 %), evident in areas where P is less accumulated, in comparison to higher grid-scale inter-product uncertainty in ET (20–55 %) spread across the entire basin. Grid-scale inter-product ΔSMS uncertainties are high in the peak rainy season due to the complex interplay of irrigation practices, monsoonal rainfall events, and the products' inherent uncertainties. The evaluations of the different products concluded the exclusion of CHIRPS-P and MOD16-ET. Analysis of the seasonal water balance across the unique P, ET, and ΔTWS realizations foster further ET fluxes exclusions per season (i.e., exclusion of MODIS-based SSEBop from the monsoon season).

In conclusion, this analysis aided in establishing a fundamental understanding of inter-product variations and appraised possibilities to improve the accuracy of input water balance components data sets. Future studies could benefit from a water balance closure approach that does not only correct the water balance components but also minimizes uncertainties in individual water balance components, as explored herein. In the case study of this analysis, a water balance closure approach that corrects and closes the water balance by incorporating 'useful' and 'internally consistent' models per season could be a way forward for improved use of the water fluxes and storages in further detailed water balance studies. In summary, excluding unreliable data sets significantly decreased the uncertainty range for each water balance component. However, for the Hindon Basin analyzed in this paper, we acknowledge the need for additional data to further reduce the uncertainties associated with the remaining unexcluded data sets. In this study, we have made a significant step towards constraining each water balance component, yet future work needs to be directed towards constraining estimates of all individual water balance terms to quantify their confident range/ distributions accurately. This will require, at a minimum, local data on river flows and external irrigation water imports. The presented work motivates the application of a grid-based multi-source data fusion technique using an ensemble approach that exploits the information content of remote sensing data to close the water balance in the Hindon basin (Mourad et al., 2024; Schoups and Nasseri, 2021).

Funding sources

This work is supported by the Dutch Research Council, Government of The Netherlands, through the Meridian Fund (project no. 482.20.303) and by the Department of Science & Technology, Government of India (project no. DST/TMDEWO/WTI/NWO/CGAW/2020/14), under the jointly funded Cleaning the Ganga and Agri-Water initiative and the Hindon Roots Sensing (HIROS) project: River Rejuvenation through Scalable Water- and Solute Balance Modelling and Informed Farmers' Actions.

Author statement

Nothing to disclose

Table 4
Range of triple collocation errors (mm/month) in individual products for P and ET fluxes and ΔSMS before and after exclusions.

	ET	P
TC range (mm/month) **(Before exclusions)**	15–38	16–52
TC range (mm/month) **(After exclusion)**	17–23	11–23

CRediT authorship contribution statement

Roya Mourad: Writing – review & editing, Writing – original draft, Visualization, Validation, Software, Resources, Methodology, Investigation, Formal analysis, Data curation, Conceptualization. **Gerrit Schoups:** Writing – review & editing, Visualization, Validation, Supervision, Resources, Project administration, Methodology, Investigation, Funding acquisition, Formal analysis, Conceptualization. **Wim Bastiaanssen:** Writing – review & editing, Visualization, Supervision, Resources, Project administration, Methodology, Investigation, Funding acquisition, Formal analysis, Data curation. **D. Nagesh Kumar:** Resources, Funding acquisition, Data curation.

Declaration of Competing Interest

The authors declare that they have no known competing financial interests or personal relationships that could have appeared to influence the work reported in this paper.

Data Availability

Data used in this study are primarily accessed through the Google Earth Engine cloud computing platform. All software used in this analysis is available at https://doi.org/10.5281/zenodo.11148992.

Acknowledgments

The authors would like to thank Dr. Martha C. Anderson (USDA-ARS) and Dr. Juan Pablo Guerschman (CSIRO) and their collaborators for developing and sharing the CMRSET and ALEXI evapotranspiration models and Tim Hessels for making these data sets accessible. The authors thank the anonymous reviewers for providing valuable comments that helped strengthen and improve the manuscript.

Appendix A. Supporting information

Supplementary data associated with this article can be found in the online version at doi:10.1016/j.ejrh.2024.101935.

References

Abatzoglou, J.T., 2013. Development of gridded surface meteorological data for ecological applications and modelling. Int. J. Climatol. 33 (1), 121–131.
Abatzoglou, J.T., Dobrowski, S.Z., Parks, S.A., Hegewisch, K.C., 2018. TerraClimate, a high-resolution global dataset of monthly climate and climatic water balance from 1958–2015. Sci. Data 5 (1), 1–12.
Abera, W., Formetta, G., Brocca, L., Rigon, R., 2017. Modeling the water budget of the Upper Blue Nile basin using the JGrass-NewAge model system and satellite data. Hydrol. Earth Syst. Sci. 21 (6), 3145–3165.
Abhishek, Kinouchi, T., Abolafia-Rosenzweig, R., Ito, M., 2021. Water budget closure in the Upper Chao Phraya River basin, Thailand using multisource data. Remote Sens. 14 (1), 173.
Abolafia-Rosenzweig, R., Pan, M., Zeng, J., Livneh, B., 2021. Remotely sensed ensembles of the terrestrial water budget over major global river basins: an assessment of three closure techniques. Remote Sens. Environ. 252, 112191.
Aires, F., 2014. Combining datasets of satellite-retrieved products. Part I: methodology and water budget closure. J. Hydrometeorol. 15 (4), 1677–1691.
Alam, F., Umar, R., 2013. Groundwater flow modelling of Hindon-Yamuna interfluve region, western Uttar Pradesh. J. Geol. Soc. India 82, 80–90.
Albergel, C., et al., 2012. Evaluation of remotely sensed and modelled soil moisture products using global ground-based in situ observations. Remote Sens. Environ. 118, 215–226.
Alemohammad, S.H., McColl, K.A., Konings, A.G., Entekhabi, D., Stoffelen, A., 2015. Characterization of precipitation product errors across the United States using multiplicative triple collocation. Hydrol. Earth Syst. Sci. 19 (8), 3489–3503.
Anderson, M.C., et al., 2015. Comparison of satellite-derived LAI and precipitation anomalies over Brazil with a thermal infrared-based Evaporative Stress Index for 2003–2013. J. Hydrol. 526, 287–302.
Anderson, M.C., Norman, J.M., Mecikalski, J.R., Otkin, J.A., Kustas, W.P., 2007. A climatological study of evapotranspiration and moisture stress across the continental United States based on thermal remote sensing: 2. Surface moisture climatology. J. Geophys. Res. Atmos. 112 (D11).
Awange, J.L., et al., 2016. Uncertainties in remotely sensed precipitation data over Africa. Int. J. Climatol. 36 (1), 303–323.
Baez-Villanueva, O.M., et al., 2018. Temporal and spatial evaluation of satellite rainfall estimates over different regions in Latin-America. Atmos. Res. 213, 34–50.

Bastiaanssen, W.G.M., 1995. Regionalization of Surface Flux Densities and Moisture Indicators in Composite Terrain: A Remote Sensing Approach under Clear Skies in Mediterranean Climates. Wageningen University and Research.

Bastiaanssen, W., Cheema, M., Immerzeel, W., Miltenburg, I., Pelgrum, H., 2012. Surface energy balance and actual evapotranspiration of the transboundary Indus Basin estimated from satellite measurements and the ETLook model. Water Resour. Res. 48 (11).

Bastiaanssen, W.G.M., Hoekman, D.H., Roebeling, R., 1993. A Methodology for the Assessment of Surface Resistance and Soil Water Storage Variability at Mesoscale Based on Remote Sensing Measurements. A Case Study with HAPEX-EFEDA data. 0926-230X. Landbouwuniversiteit Wageningen.

Bastiaanssen, W.G., Menenti, M., Feddes, R., Holtslag, A., 1998. A remote sensing surface energy balance algorithm for land (SEBAL). 1. Formulation. J. Hydrol. 212, 198–212.

Bastiaanssen, W.G., Van der Wal, T., Visser, T., 1996. Diagnosis of regional evaporation by remote sensing to support irrigation performance assessment. Irrig. Drain. Syst. 10, 1–23.

Beck, H.E., et al., 2019. MSWEP V2 global 3-hourly 0.1 precipitation: methodology and quantitative assessment. Bull. Am. Meteorol. Soc. 100 (3), 473–500.

Beria, H., Nanda, T., Singh Bisht, D., Chatterjee, C., 2017. Does the GPM mission improve the systematic error component in satellite rainfall estimates over TRMM? An evaluation at a pan-India scale. Hydrol. Earth Syst. Sci. 21 (12), 6117–6134.

Bhat, T.A., 2014. An analysis of demand and supply of water in India. J. Environ. Earth Sci. 4 (11), 67–72.

Biancamaria, S., et al., 2019. Total water storage variability from GRACE mission and hydrological models for a 50,000 km2 temperate watershed: the Garonne River basin (France). J. Hydrol. Reg. Stud. 24, 100609.

Biggs, T.W., Marshall, M., Messina, A., 2016. Mapping daily and seasonal evapotranspiration from irrigated crops using global climate grids and satellite imagery: automation and methods comparison. Water Resour. Res. 52 (9), 7311–7326.

Bolten, J.D., Crow, W.T., Zhan, X., Jackson, T.J., Reynolds, C.A., 2009a. Evaluating the utility of remotely sensed soil moisture retrievals for operational agricultural drought monitoring. IEEE J. Sel. Top. Appl. Earth Obs. Remote Sens. 3 (1), 57–66.

Bolten, J., Crow, W., 2012. Improved prediction of quasi-global vegetation conditions using remotely-sensed surface soil moisture. Geophys. Res. Lett. 39 (19).

Bolten, J.D., Crow, W.T., Zhan, X., Reynolds, C.A., Jackson, T.J., 2009b. Assimilation of A Satellite-based Soilmoisture Product Into A Two-layer Water Balance Model for A Global Crop Production Decision Support System. Data Assimilation for Atmospheric, Oceanic and Hydrologic Applications. Springer, pp. 449–463.

Cawse-Nicholson, K., et al., 2020. Sensitivity and uncertainty quantification for the ECOSTRESS evapotranspiration algorithm–DisALEXI. Int. J. Appl. Earth Obs. Geoinf. 89, 102088.

Chen, J., Wilson, C., Tapley, B., Ries, J., 2004. Low degree gravitational changes from GRACE: validation and interpretation. Geophys. Res. Lett. 31 (22).

Colliander, A., et al., 2017. Validation of SMAP surface soil moisture products with core validation sites. Remote Sens. Environ. 191, 215–231.

De Jeu, R.A., et al., 2008. Global soil moisture patterns observed by space borne microwave radiometers and scatterometers. Surv. Geophys. 29, 399–420.

De Kok, R.J., Kraaijenbrink, P.D., Tuinenburg, O.A., Bonekamp, P.N., Immerzeel, W.W., 2020. Towards understanding the pattern of glacier mass balances in high mountain Asia using regional climatic modelling. Cryosphere 14 (9), 3215–3234.

Dinerstein, E., et al., 2017. An ecoregion-based approach to protecting half the terrestrial realm. BioScience 67 (6), 534–545.

Dorigo, W.A., et al., 2010. Error characterisation of global active and passive microwave soil moisture datasets. Hydrol. Earth Syst. Sci. 14 (12), 2605–2616.

Ebert, E.E., Janowiak, J.E., Kidd, C., 2007. Comparison of near-real-time precipitation estimates from satellite observations and numerical models. Bull. Am. Meteorol. Soc. 88 (1), 47–64.

Evans, J., et al., 2012. Determination of turbulent heat fluxes using a large aperture scintillometer over undulating mixed agricultural terrain. Agric. For. Meteorol. 166, 221–233.

FAO, 2020. WaPOR Database Methodology: Version 2 Release, April 2020. FAO Rome, Itay.

Faridatul, M.I., Wu, B., Zhu, X., Wang, S., 2020. Improving remote sensing based evapotranspiration modelling in a heterogeneous urban environment. J. Hydrol. 581, 124405.

Feddes, R., Menenti, M., Kabat, P., Bastiaanssen, W., 1993. Is large-scale inverse modelling of unsaturated flow with areal average evaporation and surface soil moisture as estimated from remote sensing feasible? J. Hydrol. 143 (1-2), 125–152.

Funk, C., et al., 2015. The climate hazards infrared precipitation with stations—a new environmental record for monitoring extremes. Sci. Data 2 (1), 1–21.

Gao, H., Tang, Q., Ferguson, C.R., Wood, E.F., Lettenmaier, D.P., 2010. Estimating the water budget of major US river basins via remote sensing. Int. J. Remote Sens. 31 (14), 3955–3978.

Gehne, M., Hamill, T.M., Kiladis, G.N., Trenberth, K.E., 2016. Comparison of global precipitation estimates across a range of temporal and spatial scales. J. Clim. 29 (21), 7773–7795.

Gokmen, M., et al., 2012. Integration of soil moisture in SEBS for improving evapotranspiration estimation under water stress conditions. Remote Sens. Environ. 121, 261–274.

Guerschman, J.P., et al., 2009. Scaling of potential evapotranspiration with MODIS data reproduces flux observations and catchment water balance observations across Australia. J. Hydrol. 369 (1-2), 107–119.

Gumma, M.K., et al., 2022. Multiple agricultural cropland products of South Asia developed using Landsat-8 30 m and MODIS 250 m data using machine learning on the Google Earth Engine (GEE) cloud and spectral matching techniques (SMTs) in support of food and water security. GIScience Remote Sens. 59 (1), 1048–1077.

Han, E., Crow, W.T., Holmes, T., Bolten, J., 2014. Benchmarking a soil moisture data assimilation system for agricultural drought monitoring. J. Hydrometeorol. 15 (3), 1117–1134.

Henderson-Sellers, A., 1996. Soil moisture: a critical focus for global change studies. Glob. Planet. Change 13 (1-4), 3–9.

Herold, N., Behrangi, A., Alexander, L.V., 2017. Large uncertainties in observed daily precipitation extremes over land. J. Geophys. Res. Atmos. 122 (2), 668–681.

Hersbach, H., et al., 2020. The ERA5 global reanalysis. Q. J. R. Meteorol. Soc. 146 (730), 1999–2049.

Hessels, T., Davids, J.C., Bastiaanssen, W., 2022. Scalable water balances from earth observations (SWEO): results from 50 years of remote sensing in hydrology. Water Int. 47 (6), 866–886.

Hobbins, M., Dewes, C., Jansma, T., 2022. Global Reference Evapotranspiration for Food-Security Monitoring: US Geological Survey Data Release. US Geological Survey: Reston, VA, USA.

Hong, Y., Hsu, Kl, Moradkhani, H., Sorooshian, S., 2006. Uncertainty quantification of satellite precipitation estimation and Monte Carlo assessment of the error propagation into hydrologic response. Water Resour. Res. 42 (8).

Huffman, G.J., et al., 2007. The TRMM multisatellite precipitation analysis (TMPA): Quasi-global, multiyear, combined-sensor precipitation estimates at fine scales. J. Hydrometeorol. 8 (1), 38–55.

Huffman, G., Stocker, E., Bolvin, D., Nelkin, E., Tan, J., 2019. GPM IMERG Final Precipitation L3 1 month 0.1 degree x 0.1 degree V06. Goddard Earth Sciences Data and Information Services Center (GES DISC), Greenbelt, MD, USA.

Jaafar, H., Mourad, R., Schull, M., 2022. A Global 30-m ET Model (HSEB) Using Harmonized Landsat and Sentinel-2, MODIS and VIIRS: Comparison to ECOSTRESS ET and LST.

Jain, C., Sharma, M., 2006. Heavy metal transport in the Hindon river basin, India. Environ. Monit. Assess. 112, 255–270.

Jiang, Y., et al., 2018. Effect of cloud cover on temporal upscaling of instantaneous evapotranspiration. J. Hydrol. Eng. 23 (4), 05018002.

Karimi, P., Bastiaanssen, W.G., Molden, D., 2013. Water Accounting Plus (WA+)–a water accounting procedure for complex river basins based on satellite measurements. Hydrol. Earth Syst. Sci. 17 (7), 2459–2472.

Khan, M.S., Liaqat, U.W., Baik, J., Choi, M., 2018. Stand-alone uncertainty characterization of GLEAM, GLDAS and MOD16 evapotranspiration products using an extended triple collocation approach. Agric. For. Meteorol. 252, 256–268.

Kidd, C., Levizzani, V., 2011. Status of satellite precipitation retrievals. Hydrol. Earth Syst. Sci. 15 (4), 1109–1116.

Kim, H.W., Hwang, K., Mu, Q., Lee, S.O., Choi, M., 2012. Validation of MODIS 16 global terrestrial evapotranspiration products in various climates and land cover types in Asia. KSCE J. Civ. Eng. 16, 229–238.

Kiptala, J., Mohamed, Y., Mul, M.L., Van der Zaag, P., 2013. Mapping evapotranspiration trends using MODIS and SEBAL model in a data scarce and heterogeneous landscape in Eastern Africa. Water Resour. Res. 49 (12), 8495–8510.

Kishore, P., Singh, D.R., Srivastava, S.K., Meena, D.C., Tatipudi, B.R., 2023. Can the water rate be the only criteria to assess the viability of a canal irrigation system? a case of Eastern Yamuna Canal, India. Curr. Sci. 34–42.

Koppa, A., Gebremichael, M., 2017. A framework for validation of remotely sensed precipitation and evapotranspiration based on the Budyko hypothesis. Water Resour. Res. 53 (10), 8487–8499.

Koster, R.D., Suarez, M.J., 2001. Soil moisture memory in climate models. J. Hydrometeorol. 2 (6), 558–570.

Kumar, A., Bhatia, A., Fagodiya, R., Malyan, S., Meena, B., 2017. Eddy Covariance Flux Tower: A Promising Technique for Greenhouse Gases Measurement. Eddy Covariance Flux Tower: A Promising Technique for Greenhouse Gases Measurement.

Kustas, W., Anderson, M., 2009. Advances in thermal infrared remote sensing for land surface modeling. Agric. For. Meteorol. 149 (12), 2071–2081.

Lakshmi, V., 2016. Beyond GRACE: using satellite data for groundwater investigations. Groundwater 54 (5), 615–618.

Landerer, F.W., Swenson, S., 2012. Accuracy of scaled GRACE terrestrial water storage estimates. Water Resour. Res. 48 (4).

Lehner, B., Verdin, K., Jarvis, A., 2008. New global hydrography derived from spaceborne elevation data, Eos. Trans. Am. Geophys. Union 89 (10), 93–94.

Lewis, H., 2007. Hindon River: Gasping for Breath. Janhit Foundation, Meerut, Uttar Pradesh.

Li, B., et al., 2019a. Global GRACE data assimilation for groundwater and drought monitoring: advances and challenges. Water Resour. Res. 55 (9), 7564–7586.

Li, Y., et al., 2019c. Evaluating soil resistance formulations in thermal-based two-source energy balance (TSEB) model: implications for heterogeneous semiarid and arid regions. Water Resour. Res. 55 (2), 1059–1078.

Li, X., et al., 2019b. Evapotranspiration estimation for Tibetan Plateau headwaters using conjoint terrestrial and atmospheric water balances and multisource remote sensing. Water Resour. Res. 55 (11), 8608–8630.

Long, D., Longuevergne, L., Scanlon, B.R., 2014. Uncertainty in evapotranspiration from land surface modeling, remote sensing, and GRACE satellites. Water Resour. Res. 50 (2), 1131–1151.

Long, D., Longuevergne, L., Scanlon, B.R., 2015. Global analysis of approaches for deriving total water storage changes from GRACE satellites. Water Resour. Res. 51 (4), 2574–2594.

Luo, Z., et al., 2023. A novel two-step method for enforcing water budget closure and an intercomparison of budget closure correction methods based on satellite hydrological products. Water Resour. Res. 59 (3), e2022WR032176.

Ma, Y., et al., 2018. Estimation of daily evapotranspiration and irrigation water efficiency at a Landsat-like scale for an arid irrigation area using multi-source remote sensing data. Remote Sens. Environ. 216, 715–734.

Ma, H., et al., 2019. Satellite surface soil moisture from SMAP, SMOS, AMSR2 and ESA CCI: A comprehensive assessment using global ground-based observations. Remote Sens. Environ. 231, 111215.

Maggioni, V., Massari, C., 2018. On the performance of satellite precipitation products in riverine flood modeling: a review. J. Hydrol. 558, 214–224.

Maheswaran, R., et al., 2016. Regional scale groundwater modelling study for Ganga River basin. J. Hydrol. 541, 727–741.

Massman, W., Lee, X., 2002. Eddy covariance flux corrections and uncertainties in long-term studies of carbon and energy exchanges. Agric. For. Meteorol. 113 (1-4), 121–144.

Mekonnen, M.M., Hoekstra, A.Y., 2011. The green, blue and grey water footprint of crops and derived crop products. Hydrol. Earth Syst. Sci. 15 (5), 1577–1600.

Melton, F.S., et al., 2012. Satellite irrigation management support with the terrestrial observation and prediction system: a framework for integration of satellite and surface observations to support improvements in agricultural water resource management. IEEE J. Sel. Top. Appl. Earth Obs. Remote Sens. 5 (6), 1709–1721.

Michailovsky, C.I., Coerver, B., Mul, M., Jewitt, G., 2023. Investigating sources of variability in closing the terrestrial water balance with remote sensing. Hydrol. Earth Syst. Sci. 27 (23), 4335–4354.

Mourad, R., Schoups, G., Bastiaanssen, W., 2024. A grid-based data-driven ensemble probabilistic data fusion: a water balance closure approach applied to the irrigated Hindon River Basin, India. Copernic. Meet.

Mu, Q., Zhao, M., Running, S.W., 2011. Improvements to a MODIS global terrestrial evapotranspiration algorithm. Remote Sens. Environ. 115 (8), 1781–1800.

Mukherjee, A., Bhanja, S.N., Wada, Y., 2018. Groundwater depletion causing reduction of baseflow triggering Ganges river summer drying. Sci. Rep. 8 (1), 12049.

Niu, G.Y., et al., 2011. The community Noah land surface model with multiparameterization options (Noah-MP): 1. Model description and evaluation with local-scale measurements. J. Geophys. Res. Atmos. 116 (D12).

Otkin, J.A., Anderson, M.C., Hain, C., Svoboda, M., 2014. Examining the relationship between drought development and rapid changes in the evaporative stress index. J. Hydrometeorol. 15 (3), 938–956.

Pan, S., et al., 2020. Evaluation of global terrestrial evapotranspiration using state-of-the-art approaches in remote sensing, machine learning and land surface modeling. Hydrol. Earth Syst. Sci. 24 (3), 1485–1509.

Pan, M., Wood, E.F., 2006. Data assimilation for estimating the terrestrial water budget using a constrained ensemble Kalman filter. J. Hydrometeorol. 7 (3), 534–547.

Parinussa, R., Yilmaz, M., Anderson, M., Hain, C., De Jeu, R., 2014. An intercomparison of remotely sensed soil moisture products at various spatial scales over the Iberian Peninsula. Hydrol. Process. 28 (18), 4865–4876.

Pingali, P.L., 2012. Green revolution: impacts, limits, and the path ahead. Proc. Natl. Acad. Sci. 109 (31), 12302–12308.

Priestley, C.H.B., Taylor, R.J., 1972. On the assessment of surface heat flux and evaporation using large-scale parameters. Mon. Weather Rev. 100 (2), 81–92.

Qin, J., et al., 2013. Spatial upscaling of in-situ soil moisture measurements based on MODIS-derived apparent thermal inertia. Remote Sens. Environ. 138, 1–9.

Rodell, M., et al., 2004. The global land data assimilation system. Bull. Am. Meteorol. Soc. 85 (3), 381–394.

Rodell, M., Velicogna, I., Famiglietti, J.S., 2009. Satellite-based estimates of groundwater depletion in India. Nature 460 (7258), 999–1002.

Running, S.W., Mu, Q., Zhao, M., Moreno, A., 2017. MODIS gLobal Terrestrial Evapotranspiration (ET) Product (NASA MOD16A2/A3) NASA Earth Observing System MODIS Land Algorithm. NASA: Washington, DC, USA.

Sachar, P., 2015. Irrigation water demand for the Hindon Basin: Uttar Pradesh, India. Spat. Divers. Dyn. Resour. Urban Dev. Vol. 1 Reg. Resour. 341–360.

Sarojini, B.B., Stott, P.A., Black, E., 2016. Detection and attribution of human influence on regional precipitation. Nat. Clim. Change 6 (7), 669–675.

Save, H., Bettadpur, S., Tapley, B.D., 2016. High-resolution CSR GRACE RL05 mascons. J. Geophys. Res. Solid Earth 121 (10), 7547–7569.

Scanlon, B.R., et al., 2016. Global evaluation of new GRACE mascon products for hydrologic applications. Water Resour. Res. 52 (12), 9412–9429.

Scanlon, B., et al., 2019. Tracking seasonal fluctuations in land water storage using global models and GRACE satellites. Geophys. Res. Lett. 46 (10), 5254–5264.

Schoups, G., Nasseri, M., 2021. GRACEfully closing the water balance: a data-driven probabilistic approach applied to river basins in Iran. Water Resour. Res. 57 (6), e2020WR029071.

Scipal, K., Holmes, T., De Jeu, R., Naeimi, V., Wagner, W., 2008. A possible solution for the problem of estimating the error structure of global soil moisture data sets. Geophys. Res. Lett. 35 (24).

Senay, G.B., et al., 2013. Operational evapotranspiration mapping using remote sensing and weather datasets: a new parameterization for the SSEB approach. JAWRA J. Am. Water Resour. Assoc. 49 (3), 577–591.

Senay, G.B., 2018. Satellite psychrometric formulation of the operational simplified surface energy balance (SSEBop) model for quantifying and mapping evapotranspiration. Appl. Eng. Agric. 34 (3), 555–566.

Senay, G.B., et al., 2023. Improving the operational simplified surface energy balance evapotranspiration model using the forcing and normalizing operation. Remote Sens. 15 (1), 260.

Seo, D., Lakhankar, T., Khanbilvardi, R., 2010. Sensitivity analysis of b-factor in microwave emission model for soil moisture retrieval: a case study for SMAP mission. Remote Sens. 2 (5), 1273–1286.

Sheffield, J., Ferguson, C.R., Troy, T.J., Wood, E.F., McCabe, M.F., 2009. Closing the terrestrial water budget from satellite remote sensing. Geophys. Res. Lett. 36 (7).

Sheffield, J., Wood, E.F., 2007. Characteristics of global and regional drought, 1950–2000: analysis of soil moisture data from off-line simulation of the terrestrial hydrologic cycle. J. Geophys. Res. Atmos. 112 (D17).

Soltani, S.S., Ataie-Ashtiani, B., Danesh-Yazdi, M., Simmons, C.T., 2020. A probabilistic framework for water budget estimation in low runoff regions: a case study of the central Basin of Iran. J. Hydrol. 586, 124898.

Sriwongsitanon, N., et al., 2020. Validation of seven global remotely sensed ET products across Thailand using water balance measurements and land use classifications. J. Hydrol. Reg. Stud. 30, 100709.

Stoffelen, A., 1998. Toward the true near-surface wind speed: error modeling and calibration using triple collocation. J. Geophys. Res. Oceans 103 (C4), 7755–7766.

Sun, Q., et al., 2018. A review of global precipitation data sets: data sources, estimation, and intercomparisons. Rev. Geophys. 56 (1), 79–107.

Swenson, S., Wahr, J., 2002. Methods for inferring regional surface-mass anomalies from Gravity Recovery and Climate Experiment (GRACE) measurements of time-variable gravity. J. Geophys. Res. Solid Earth 107 (B9). ETG 3-1-ETG 3-13.

Swenson, S., Wahr, J., 2006. Post-processing removal of correlated errors in GRACE data. Geophys. Res. Lett. 33 (8).

Taylor, R.G., et al., 2013. Ground water and climate change. Nat. Clim. Change 3 (4), 322–329.

Thornton, M. et al., 1840. Daymet: Daily Surface Weather Data on a 1-km grid for North America, Version 4. ORNL DAAC, Oak Ridge, Tennessee, USA.

Tuinenburg, O., de Vries, J., 2017. Irrigation patterns resemble ERA-Interim reanalysis soil moisture additions. Geophys. Res. Lett. 44 (20), 10,341–10,348.

Vanham, D., et al., 2018. Physical water scarcity metrics for monitoring progress towards SDG target 6.4: an evaluation of indicator 6.4. 2 "Level of water stress". Sci. Total Environ. 613, 218–232.

Velpuri, N.M., Senay, G.B., Singh, R.K., Bohms, S., Verdin, J.P., 2013. A comprehensive evaluation of two MODIS evapotranspiration products over the conterminous United States: using point and gridded FLUXNET and water balance ET. Remote Sens. Environ. 139, 35–49.

Vishwakarma, B.D., Devaraju, B., Sneeuw, N., 2018. What is the spatial resolution of GRACE satellite products for hydrology? Remote Sens. 10 (6), 852.

Wahr, J., Molenaar, M., Bryan, F., 1998. Time variability of the Earth's gravity field: hydrological and oceanic effects and their possible detection using GRACE. J. Geophys. Res. Solid Earth 103 (B12), 30205–30229.

Walker, J.P., Houser, P.R., 2001. A methodology for initializing soil moisture in a global climate model: assimilation of near-surface soil moisture observations. J. Geophys. Res. Atmos. 106 (D11), 11761–11774.

Wang, W., Huang, D., Wang, X., Liu, Y., Zhou, F., 2010. Estimate soil moisture using trapezoidal relationship between remotely sensed land surface temperature and vegetation index. Hydrol. Earth Syst. Sci. Discuss. 7, 8703–8740.

Wang-Erlandsson, L., et al., 2016. Global root zone storage capacity from satellite-based evaporation. Hydrol. Earth Syst. Sci. 20 (4), 1459–1481.

Watkins, M.M., Wiese, D.N., Yuan, D.N., Boening, C., Landerer, F.W., 2015. Improved methods for observing Earth's time variable mass distribution with GRACE using spherical cap mascons. J. Geophys. Res. Solid Earth 120 (4), 2648–2671.

Weerasinghe, I., Bastiaanssen, W., Mul, M., Jia, L., Van Griensven, A., 2020. Can we trust remote sensing evapotranspiration products over Africa? Hydrol. Earth Syst. Sci. 24 (3), 1565–1586.

Wiese, D.N., Landerer, F.W., Watkins, M.M., 2016. Quantifying and reducing leakage errors in the JPL RL05M GRACE mascon solution. Water Resour. Res. 52 (9), 7490–7502.

Wong, J.S., et al., 2021. Assessing water balance closure using multiple data assimilation–and remote sensing–based datasets for canada. J. Hydrometeorol. 22 (6), 1569–1589.

Wood, E.F., et al., 2011. Hyperresolution global land surface modeling: meeting a grand challenge for monitoring Earth's terrestrial water. Water Resour. Res. 47 (5).

Xu, R., et al., 2017. Ground validation of GPM IMERG and TRMM 3B42V7 rainfall products over southern Tibetan Plateau based on a high-density rain gauge network. J. Geophys. Res. Atmos. 122 (2), 910–924.

Yang, Y., et al., 2015. Comparison of three dual-source remote sensing evapotranspiration models during the MUSOEXE-12 campaign: revisit of model physics. Water Resour. Res. 51 (5), 3145–3165.

Yang, S., Zeng, J., Fan, W., Cui, Y., 2022. Evaluating root-zone soil moisture products from GLEAM, GLDAS, and ERA5 based on in situ observations and triple collocation method over the Tibetan Plateau. J. Hydrometeorol. 23 (12), 1861–1878.

Yilmaz, M.T., Crow, W.T., 2013. The optimality of potential rescaling approaches in land data assimilation. J. Hydrometeorol. 14 (2), 650–660.

Zambrano-Bigiarini, M., Nauditt, A., Birkel, C., Verbist, K., Ribbe, L., 2017. Temporal and spatial evaluation of satellite-based rainfall estimates across the complex topographical and climatic gradients of Chile. Hydrol. Earth Syst. Sci. 21 (2), 1295–1320.

Zanaga, D. et al., 2022. ESA WorldCover 10 m 2021 v200.

Zhang, Y., et al., 2018. A Climate Data Record (CDR) for the global terrestrial water budget: 1984–2010. Hydrol. Earth Syst. Sci. 22 (1), 241–263.

Zhang, A., et al., 2019. Evaluation of latest GPM-Era high-resolution satellite precipitation products during the May 2017 Guangdong extreme rainfall event. Atmos. Res. 216, 76–85.

Zomer, R.J., Xu, J., Trabucco, A., 2022. Version 3 of the global aridity index and potential evapotranspiration database. Sci. Data 9 (1), 409.